# Using Wind Dispersion Effects During the InSight Tether Burial Activities to Better Constrain the Regolith Grain Size Distribution

Nicolas Verdier, V. Ansan, P. Delage, K S Ali, E. Beucler, C. Charalambous, E. Constant, A. Spiga, M. Golombek, E. Marteau, et al.

JGR Planets

RESEARCH ARTICLE
10.1029/2022JE007707

**Key Points:**

- The grain size distribution of the InSight Martian regolith is better constrained by using wind as a sorter during the burial of a tether
- Based on image observations and numerical fluid mechanics simulations, the regolith mainly contains grains between 100 µm and 1 mm
- Grains smaller than 100 µm are not quantifiable because they have been blown away by the wind

**Correspondence to:**
N. Verdier,
nicolas.verdier@cnes.fr

**Citation:**
Verdier, N., Ansan, V., Delage, P., Ali, K. S., Beucler, E., Charalambous, C., et al. (2023). Using wind dispersion effects during the InSight tether burial activities to better constrain the regolith grain size distribution. *Journal of Geophysical Research: Planets*, *128*, e2022JE007707. https://doi.org/10.1029/2022JE007707

Received 9 DEC 2022
Accepted 31 MAR 2023



# Using Wind Dispersion Effects During the InSight Tether Burial Activities to Better Constrain the Regolith Grain Size Distribution

**N. Verdier[1], V. Ansan[2], P. Delage[3], K. S. Ali[4], E. Beucler[2], C. Charalambous[5], E. Constant[6], A. Spiga[7], M. Golombek[4], E. Marteau[4], R. Lapeyre[1], E. Gaudin[1], C. Yana[1], K. Hurst[4], P. Lognonné[8], and B. W. Banerdt[4]**

[1]Centre National d'Etudes Spatiales, Toulouse, France, [2]Laboratoire Planétologie et Géosciences (LPG), UMR6112 CNRS, Nantes Université, Nantes, France, [3]Ecole des Ponts ParisTech, Laboratoire Navier (CERMES), CNRS, Paris, France, [4]Jet Propulsion Laboratory, NASA-California Institute of Technology, Pasadena, CA, USA, [5]Imperial College, London, UK, [6]R.Tech, Parc Technologique Delta Sud, Verniolle, France, [7]Laboratoire de Météorologie Dynamique, IPSL, Sorbonne Université, CNRS, Paris, France, [8]Université Paris-Cité, Institut de Physique du Globe de Paris, CNRS, Paris, France

**Abstract** In an attempt to improve the quality of the seismic signals provided by the seismometer of the InSight mission (**In**terior Exploration using **S**eismic **I**nvestigations, **G**eodesy and **H**eat **T**ransport) on Mars, part of the tether linking the seismometer to the InSight lander was buried by some regolith using the scoop of the articulated robotic arm. The regolith in a source area was scraped into piles, scooped and dumped by the scoop from a height of ∼50 cm above the surface onto the tether. Part of the regolith was carried away by the wind and dispersed 1–2 m downwind, as evidenced by the comparison between images taken from the lander before and after the regolith pouring. Using both ballistic trajectory and wind dispersion effects as a sorter, the grain size range was determined through numerical fluid mechanics simulations. The trajectory of the poured grains is determined by the Martian atmospheric and gravimetry conditions, the initial conditions of scoop pouring and grain lithology. The spatial grain distribution on the ground shows a downwind decrease in grain size from the pouring point, with a size ranging from 1 mm near the dump point to ∼100 µm at the farthest area observed on the images. We find that the deposit of grains coarser than 500 µm is controlled mainly by gravity. Grains finer than 100 µm are present in the regolith, but they are not quantifiable with this method because they are blown away by the wind.

**Plain Language Summary** The soil on which the lander of the geophysical InSight mission on Mars has landed is partially known, mainly through visual observations by the lander's cameras and calculations based on their thermal properties (derived from both orbiter and lander measurements). Some soil scraped by the scoop of the lander's robotic arm was dumped on the tether connecting the InSight seismometer, so as to improve the quality of the seismic signals. During these dumpings, it was observed that some particles were blown away by Martian winds that were simultaneously recorded by the lander instruments. Given that they are subjected to the combined effect of gravity and wind, larger particles rapidly fall below the scoop, whereas smaller ones are blown away; the smaller the particle, the larger the distance. The trajectory of the poured particles was numerically calculated using fluid mechanics to account for wind effects, and the resulting downwind deposit was compared to that given by photos. It was shown that particles larger than 500 µm fell close to the pile formed below the scoop, whereas smaller ones (>100 µm) fell at distances of 2–4 m. Smaller particles (<100 µm) including dust (<5–10 µm) were blown further away.

## 1. Introduction

InSight (**In**terior Exploration using **S**eismic **I**nvestigations, **G**eodesy and **H**eat **T**ransport) is a Mars geophysical lander (Banerdt et al., 2020), managed by NASA with European space agencies (e.g., CNES—Center National d'Etudes Spatiales, France and DLR—Deutschen Zentrum für Luft- und Raumfahrt, Germany) payload contributions that touched down on the Western Elysium Planitia on Mars, on 26 November 2018. InSight aims at better understanding the structure of the planet through, among other instruments, the very sensitive SEIS seismometer (Seismic Experiment for Internal Structure, Lognonné et al., 2019). By analyzing signals from marsquakes (e.g., Banerdt et al., 2020; Giardini et al., 2020; Lognonné et al., 2020) and meteor activity (e.g., Garcia et al., 2022; Posiolova et al., 2022), the knowledge of Mars' structure has been significantly improved from the upper crust

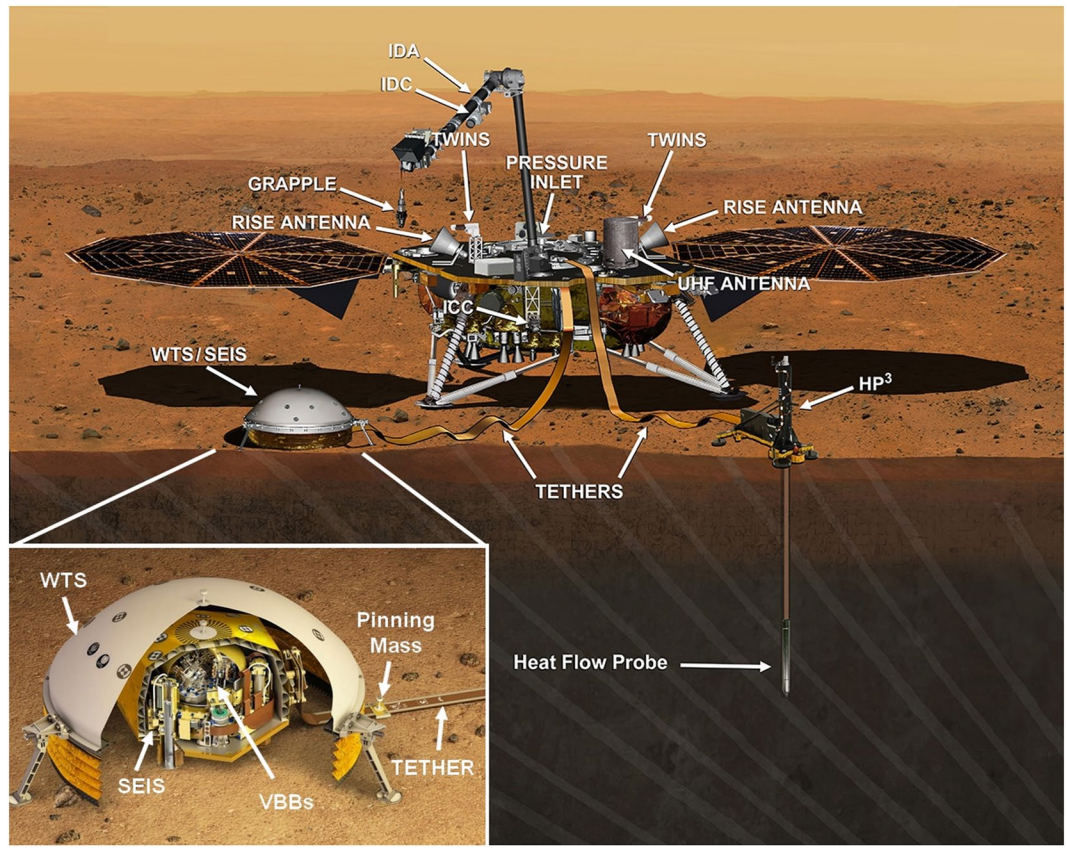


**Figure 1.** Artist view of the InSight lander and SEIS instrument (credit NASA –InSight mission and IPGP D.Ducros).

down to the core (Khan et al., 2021; Knapmeyer-Endrun et al., 2021; Lognonné et al., 2020; Stähler et al., 2021). Reviews of SEIS results can be found in Lognonné et al. (2023), Knapmeyer-Endrun et al. (2022), and Giardini et al. (2022).

Figure 1 shows an artist's view of the InSight lander with both the SEIS instrument (covered by Wind and Thermal Shield—WTS) and the Heat flow and Physical Properties Package ($HP^3$ instrument, Spohn et al., 2018) with the thermal probe penetrated into the soil. Both instruments are connected to the lander by tethers that provide energy and transmit data. They were placed on the surface by the Instrument Deployment Arm (IDA, Trebbi-Ollenu et al., 2018), on which is fixed the Instrument Deployment Camera (IDC, Maki et al., 2018) and a scoop at its end that can be rotated by the wrist joint. In addition, the lander is equipped with temperature and wind sensors (TWINS) similar to the ones performed onboard Curiosity rover (Gómez-Elvira et al., 2012) described in Banfield et al. (2020) and an Instrument Context Camera (ICC, Maki et al., 2018). Energy is provided by two solar arrays (1.8 m diameter, 700 W power when they are clean and on clear days). Progressive dust accumulation on the arrays (Lorenz et al., 2021) resulted in the end of the mission for lack of energy on 15 December 2022.

InSight landed within a 27-m diameter depression with a relatively smooth surface dotted with some centimeter-sized pebbles without aeolian bedforms (Golombek, Warner, et al., 2020; Golombek, Williams, et al., 2020; Warner et al., 2020, 2022), in spite of permanent wind (Banfield et al., 2019, 2020). Previous estimations of the average grain size at the surface from thermal inertia values measured by the THEMIS (Thermal Emission Imaging System, Christensen et al., 2004) instrument, on Mars Odyssey spacecraft, provided values between 160 and 230 $J.m^{-2}.K^{-1}.s^{-1/2}$, corresponding to an average diameter of 170 μm categorized as fine sand (Golombek et al., 2018). The $HP^3$ thermal probe measured a thermal conductivity of $0.041 \pm 0.013$ $W.m^{-1}.K^{-1}$ at surface, resulting in a density estimated around 1,200 $kg.m^{-3}$, a rather low value (Grott et al., 2021). During landing, pulsed retrorockets removed surficial fine-grained particles and scoured granular material away from the lander to a depth of less than 1 cm around, suggesting that the surface material was composed of loose sand and granules (Golombek, Warner, et al., 2020; Golombek, Williams, et al., 2020; Weitz et al., 2020). In

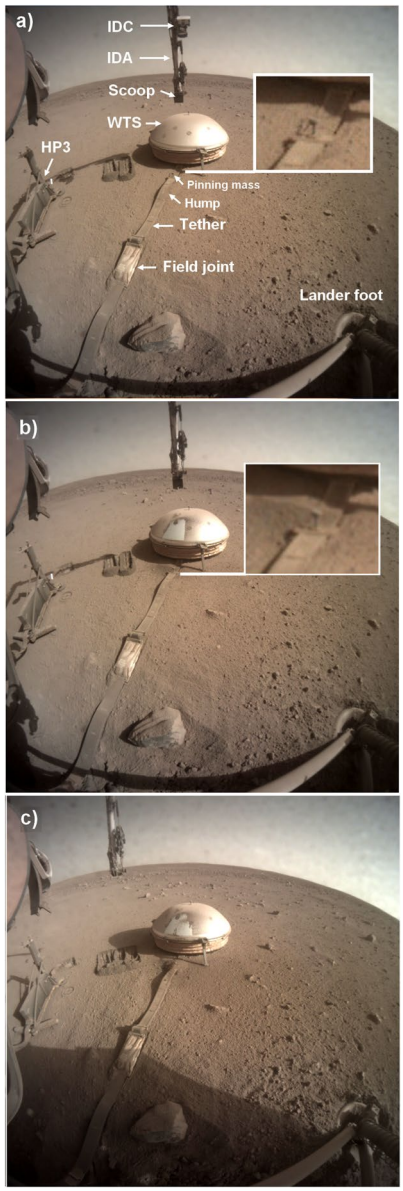


**Figure 2.** Images taken by the Instrument Context Camera at different steps of the tether burial operations. (a) Image taken on 14 March 2021, Sol 816 of the InSight mission (local mean solar time—LMST—was 15:33:15.648 p.m.). Note the arrow indicating the tether hump above the ground. Some dust stuck all over the WTS is observed; (b) Image taken at 15:37:09.227 p.m. (Sol 816), few minutes after the first regolith dump. Note the cleaning of the WTS resulting from the dumped regolith flowing over the WTS. (c) Image taken on 16 May 2021 (Sol 877) at 16:30:39.688 p.m., after the sixth dump, with more scrapes observed at the left of the WTS.

addition, pits (up to 10 cm deep) observed beneath the retro rockets and around the partially penetrated HP$^3$ mole showed steep walls and overhangs with small pebbles cemented in a cohesive finer grained matrix called duricrust (Delage et al., 2022; Marteau et al., 2022; Spohn, Hudson, Marteau, et al., 2022; Spohn, Hudson, Witte, et al., 2022; Warner et al., 2022).

Regolith results from the interaction of several surface processes, such as meteor impacts, weathering, erosion, grain saltation, and sorting by gravity and winds; it thus offers a unique opportunity to constrain the mechanics of these processes. There are few ground observations of grain-size distributions in Martian regolith. They show a great diversity of sizes ranging from blocks to sandy particles (e.g., at Viking landing sites (e.g., Mutch et al., 1976; Shorthill et al., 1976)), at Mars Pathfinder site (e.g., Moore et al., 1999; Yingst et al., 2007), at Spirit site (e.g., Grant et al., 2004; Ward et al., 2005), at Opportunity site (e.g., Weitz et al., 2006), at Phoenix site (e.g., Heet et al., 2009) and at Curiosity site (e.g., Weitz et al., 2018; Yingst et al., 2013). However, few quantitative constraints of the regolith grain-size distributions have been carried out in situ on Mars, in particular for fine grains.

Since the first observations made with the photos provided by the Viking landers'cameras (e.g., Moore & Jakoski, 1989), various estimations of the regolith grain sizes, ranging from few μm to few cm, were made on various surfaces, including aeolian bedforms. Data from orbiters (e.g., Lane & Christensen, 2013; Rogers & Bandfield, 2009) and cameras onboard rovers with sufficient resolution (e.g., Ehlmann et al., 2017; Jerolmack et al., 2006; Sullivan & Kok, 2017; Sullivan et al., 2005, 2008; Weitz et al., 2018) have shown that most of the Martian aeolian bedforms observed are composed of 50 to 2,000 μm subrounded/rounded grains (e.g., Gough et al., 2021; Sullivan et al., 2005, 2008; Weitz et al., 2018), with a preferential range of 50–350 μm for mobile active grains in ripples.

Although not planned at the beginning of the mission, an opportunity to further constrain the grain size distribution (GSD) of the granular surface regolith (few centimeters deep) occurred during the burial process of the tether connecting the seismometer to the lander. Burial was carried out with the scoop of IDA (Golombek et al., 2023; Yana et al., 2021, 2023) so as to reduce glitches (Scholz et al., 2020) in the seismic signals by improving the tether thermal insulation. Burying consisted of scraping, shovelling and dumping the surface regolith above the tether. This paper describes how the GSD of regolith was further constrained due to sorting by wind and gravity. This was done based on fluid mechanics calculations and quantifications of the regolith dumped either in piles or deposited along downstream plumes that were observed on images.

## 2. Operational Context and Analysis of Regolith From Spacecraft Data

Tether burial was monitored by two 1,024 × 1,024 pixel color cameras with a millimeter spatial resolution (Maki et al., 2018). The ICC is mounted on the underside of the lander deck (Figure 1) with its "fisheye" field of view (FOV) 120° wide pointed toward south of the lander, monitoring the instruments deployed on the Martian ground (Figure 2). The IDC, mounted on the forearm near the elbow of the IDA (Figure 1), provides a panoramic view of the terrain surrounding the landing site by moving the arm (Trebi-Ollennu et al., 2018). It allows typical ground stand-off distances to capture images at 1 mm.pixel$^{-1}$ (Maki et al., 2018). When the robotic arm's scoop is placed on the surface, the IDC can achieve its closest position to the surface at a height of 0.65 m, with the best resolution of 0.53 mm.pixel$^{-1}$.

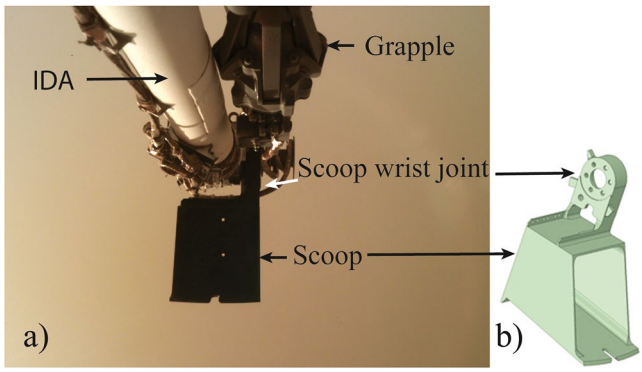


**Figure 3.** (a) This image was acquired by IDC on 5 December 2018, Sol 8 of the InSight mission. It shows the wrist of the robotic arm (Instrument Deployment Arm) with the grapple (i.e., the 5-finger clip) and the scoop. (b) Sketch of the 7.6-cm-wide scoop with a notch in the front edge. The scoop can rotate around a horizontal axis at the wrist joint at the top of the scoop.

As observed on the ICC images (Figure 2), the tether connecting the lander to the seismometer is fixed to the soil by means of a 288-g pinning mass. Between the pining mass and the field joint (i.e., the connection between the two tether sections, one from the lander and one from the seismometer), a tether hump (indicated by a white arrow) is observed, breaking the tether adhesion on the ground (Figure 2). This hump is suspected to be at the origin of recurrent, short but large signals (i.e., glitches) polluting the SEIS data. The back-azimuth source for some of them pointed toward the lander and the tether, especially during late afternoon when the temperature drop causes a thermal contraction of the tether (Scholz et al., 2020). The hump is also suspected to result in a significant sensitivity with respect to Martian winds that can reach velocities up to 20 $m.s^{-1}$ during gusts 1 m above ground, as measured by the wind sensors (Banfield et al., 2020; Spiga et al., 2021). It was considered that both thermal and wind issues could be solved by covering the tether by a layer of regolith scraped and poured by the IDA scoop. As shown in Figure 2b, regolith extraction could be done because of the low cohesion of the surface material over the first few centimeters of depth (Golombek, Warner, et al., 2020; Golombek, Williams, et al., 2020; Spohn, Hudson, Marteau, et al., 2022; Warner et al., 2022). The surface material would be composed of sand and loose granules (Golombek, Warner, et al., 2020; Golombek, Williams, et al., 2020; Weitz et al., 2020), but the exact GSD could not be further quantified due to the insufficient spatial resolution of IDC images (i.e., >0.5 mm.pixel-1 for the very close range IDC images). As aphelion was approaching, the power supplied by the solar arrays was decreasing due to dust cover coming from dust storms (Banfield et al., 2020; Beish, 2023). It was decided to make the most of what was possible before the power was too low to support the robotic activities of the IDA movement. To guarantee a sufficient volume of regolith dumped on the tether, the tether burial operations required four steps: (a) scraping enough regolith to form piles; (b) scooping the regolith into the shovel; (c) carrying it over the tether (shoveling phase); and (d) dumping it as accurately as possible onto the tether, taking into account wind conditions. They were planned and carried out (Golombek et al., 2023; Yana et al., 2021, 2023) from 28 February 2021 (sol 803) to 16 May 2021 (sol 877), with six dumps beginning at sol 216 (Figure 2b). Only the last four were considered for the grain size assessment because the two first ones were dumped on the WTS. The covering was partially successful, with the tether covered between the hump and the WTS (sol 877, Figure 2c).

### 2.1. Scraping

Scraping was carried out by using the scoop fixed at the extremity of the IDA (Figure 3). The scoop is 7.6 cm wide with a notch in the middle of the front edge. It can rotate around the wrist joint, allowing for scraping, shoveling and pouring the regolith from a height that was fixed at 45 cm.

Prior to the six dumps, six scraps were performed east of the WTS, as seen in Figure 4a. Due to better lighting, Figure 4b clearly shows the shape of the trenches with the imprint of the notch in the middle of the trenches. One can also see, at their end, the conical shaped piles of regolith pushed by the scoop. The surface material mobilized using this process is made up mostly of fine-grained material (i.e., <0.5 mm in diameter) with few pebbles.

By moving the robotic arm (Trebi-Ollennu et al., 2018), IDC images are acquired at different positions, with a horizontal post spacing ranging from 0.5 to 2 $mm.pixel^{-1}$ (Abarca et al., 2019; Maki et al., 2018). These ground data are mosaicked and projected in Cartesian coordinates in the lander frame (see Abarca et al., 2019 for details), with local height oriented downwards. This provides mosaics of orthorectified images and Digital Elevation Models (DEM) with a gridding of 1 $mm.pixel^{-1}$ and height accuracy of 1 mm for areas near the lander. However, the heights of some areas on the DEMs may be inaccurate due to shadows that affected the stereo correlations and disparities in the mean slope of the DEMs. In order to minimize these effects, the shadowed areas were removed from the volume calculations. An accurate estimation of the shape of the trenches and piles was made by DEM (Figure 4c), that showed that each excavated trench has an area around 8 cm wide and 25 cm long, with an average depth of 1.5 cm.

The volume of scraped regolith was calculated from the DEM differencing between each scraping. To minimize the effect of average slope on each DTM in the volume calculation, relative restoration of heights was performed locally by taking homologous points located a few centimeters around the area (points that were not affected

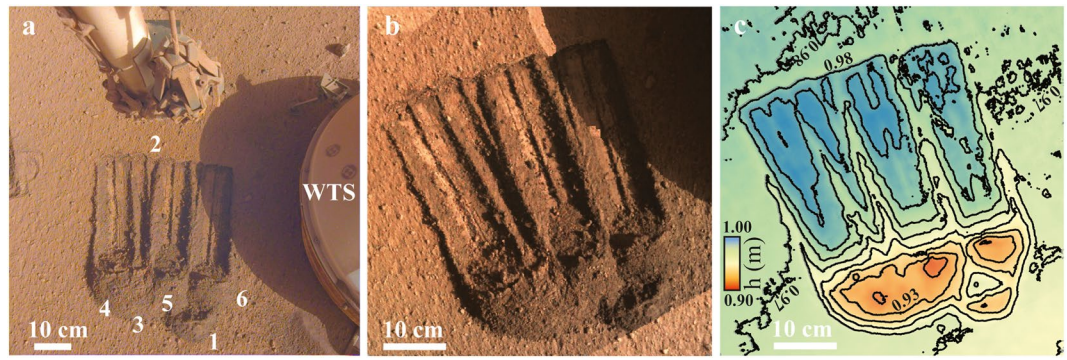


**Figure 4.** (a) IDC Photo of the 6 trenches of regolith scraped by the scoop (sol 829 at 15h20), acquired by the IDC camera mounted on the robotic arm. The trenches are located on the east side of the SEIS wind shield (WTS). A pile of regolith is generated by scraping the top layer of unconsolidated clastic soil with the tip of the scoop. Numbers correspond to scraping order. (b) A mosaic of orthorectified images is performed with a spatial resolution of 1 mm.pixel$^{-1}$. (c) An associated Digital Elavation Models shows the topography of the area with a gridding size of 1 mm.pixel$^{-1}$. The height h (oriented downwards) is given in meters with an accuracy of 1 mm. The interval of contour lines is 1 cm. Blue is trench area and red is pile area.

by the deposition or excavation of regolith between the two DTMs). To calculate the volume uncertainty, a 2-mm-wide buffer was defined around the deposit or excavation area due to the imprecision of the area bordering. Then, the volume was calculated over the whole area, including the buffer, by differentiating the DTMs before/after deposition or excavation. The difference in the volumes, including or not the buffer, corresponds to the volume uncertainty. The volumes of troughs and ridges at the end of scraping are reported in Table 1. The total volume of regolith available from the six dumps carried out for tether burial is 1,745.6 ± 407.1 cm$^3$.

### 2.2. Shoveling

The processes of shoveling and dumping are described in Figure 5. Once the trenches and piles are made, some regolith was shoveled from the piles by the scoop by first moving the IDA and the scoop close to the terrain, with the back of the scoop approximately parallel to the surface (Figure 5, 11h04). Then, the scoop was moved into the pile of regolith by rotating only the IDA elbow joint (11h08). Finally, the wrist joint was rotated to trap the regolith into the bucket of the scoop (11h12).

As the arm does not have a sensor to measure the mass of the regolith contained in the scoop, it was necessary to estimate the volume contained in the scoop from the difference in DEMs before and after shoveling, as seen in Figure 6 (last shovelful (6) carried out on day 877). Figures 6a and 6b are orthorectified images prior (sol 870) and after (sol 877) shoveling #6 respectively, with a larger view also taken on sol 877 (Figure 6c). In the associated DEMs (Figures 6d and 6e, respectively), the area of extracted regolith is outlined by the dashed red lines derived from the differentiated DEMs presented in Figure 6f. During shoveling #6, the regolith was extracted from a bump of 4 cm height, covering a surface of ∼12 cm × 8 cm (Figure 6d).

To evaluate the extracted volume, the volume of the ridge formed in front of the scoop was substracted from the volume of the trough (see Table 2). However, the volume contained in the scoop is not very well constrained due to the noise of the DEMs, the precision of their height (1 mm for each pixel), and the spatial delimitation of the extraction area whose width is estimated to be close to 2 mm. The average volume contained in the scoop is around 100 cm$^3$, with a total volume reaching 652.5 ± 326.8 cm$^3$ for the six shovelings.

**Table 1**
*Volumes of Troughs and Ridges During Scraping Step*

| | Sol 803 | Sol 803 | Sol 822 | Sol 822 | Sol 829 | Sol 851 |
|---|---|---|---|---|---|---|
| | Scrap1 | Scrap2 | Scrap3 | Scrap4 | Scrap5 | Scrap6 |
| Ridge (cm$^3$) | 285.3 ± 60.6 | 367.3 ± 65.4 | 214.3 ± 95.0 | 275.5 ± 67.3 | 376.6 ± 75.8 | 226.5 ± 43.0 |
| Trough (cm$^3$) | 254.0 ± 61.2 | 324.2 ± 60.8 | 210.0 ± 84.0 | 201.2 ± 40.1 | 315.0 ± 50.4 | 184.0 ± 59.6 |

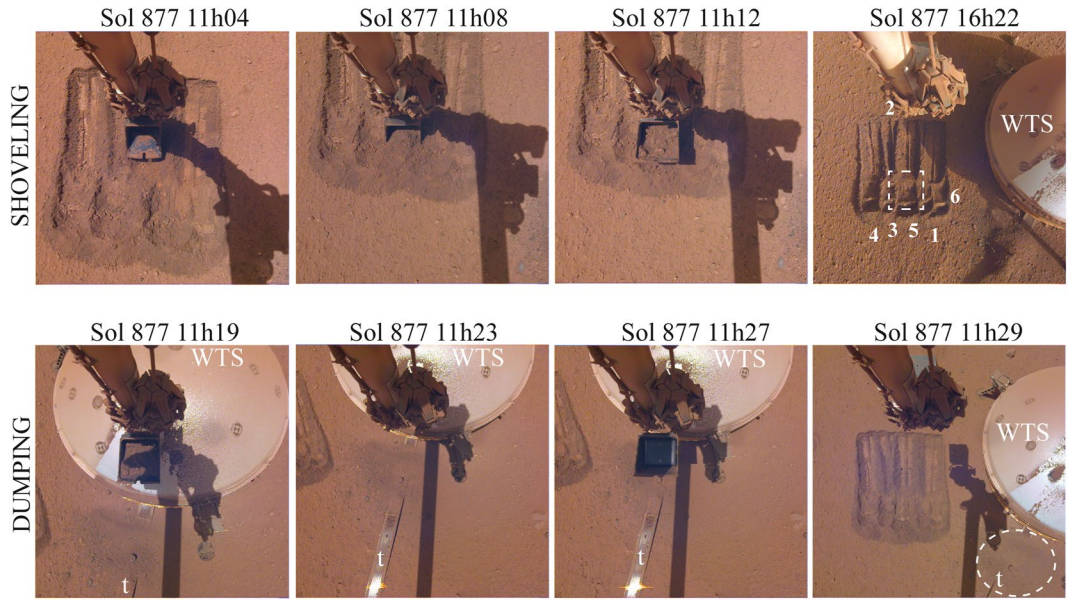


**Figure 5.** Process timeline for dump 6 through IDC images taken on sol 877: The Instrument Deployment Arm moves the scoop to extract regolith (11h04–11h08–11h12). Then, it carries regolith above the SEIS tether (t on image) at 11h19 before dumping it (11h23). Dashed contours are the location of shoveling (11h12) and dumping (11h23) areas, captured by the IDC later (16h22). One can still see the pin fixing the tether to the soil in the middle of the pile of dumped regolith (11h29).

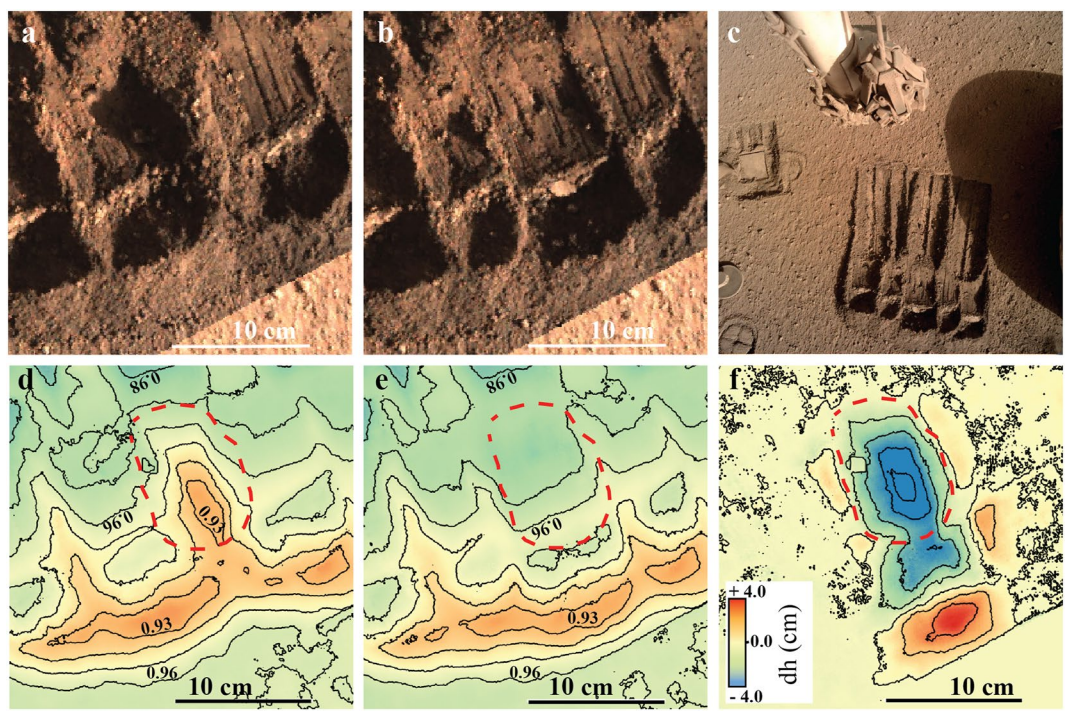


**Figure 6.** Quantification of the volume extracted by the scoop during dump 6. (a) Orthorectified IDC image taken on sol 870 before shoveling. (b) Orthorectified IDC image, sol 877 after shoveling. (c) IDC image acquired on 16 May 2021, Sol 877 (local mean solar time for the image exposure was 16:06:13.981 p.m.). The scoop-extracted regolith is located at the center of scraping areas (dashed red line contour). Images d and e represent DEMs generated from IDC images (a) and (b). (e) Digital Elavation Models differencing showing the area of regolith extracted by scoop. The interval of contour lines is 1 cm.

**Table 2**
*Volume of Regolith Extracted and Dumped by the Scoop Calculated From Digital Elavation Models Differencing*

| | SOL 816 | SOL851 | SOL857 | SOL864 | SOL870 | SOL877 |
|---|---|---|---|---|---|---|
| | Shovel1 | Shovel2 | Shovel3 | Shovel4 | Shovel5 | Shovel6 |
| Ridge volume ($cm^3$) | 108.2 ± 26.4 | 119.7 ± 30.4 | 91.7 ± 30.1 | 76.1 ± 18.1 | 45.9 ± 24.4 | 60.4 ± 21.6 |
| Trough volume ($cm^3$) | 210.2 ± 27.1 | 183.0 ± 26.1 | 167.3 ± 24.0 | 272.8 ± 38.7 | 135.1 ± 27.3 | 186.2 ± 32.4 |
| Scoop volume (ridge - trough) ($cm^3$) | 102.0 ± 53.5 | 63.2 ± 56.5 | 75.6 ± 54.2 | 196.7 ± 56.8 | 89.2 ± 51.8 | 125.8 ± 54.0 |
| | DUMP1 | DUMP2 | DUMP3 | DUMP4 | DUMP5 | DUMP6 |
| Pile volume ($cm^3$) | 61.8 ± 29.0 | 52.0 ± 35.9 | 56.9 ± 26.7 | 102.7 ± 56.7 | 44.2 ± 37.9 | 71.4 ± 48.1 |
| Dispersed material (pile - scoop) ($cm^3$) | 40.2 ± 82.5 | 11.2 ± 92.5 | 18.6 ± 80.9 | 94.0 ± 113.5 | 44.9 ± 89.7 | 54.4 ± 102.1 |
| % volume dispersed material (dispersed/scoop) | 39.40 | 17.78 | 24.64 | 47.79 | 50.41 | 43.23 |

### 2.3. Dumping

Many trial tests were necessary prior to successfully dumping the regolith over the tether due to various issues. First of all, technical difficulties were met with respect to: (a) the movement of the arm; (b) the rotation of the scoop along the wrist joint to dump the regolith without touching the WTS; and (c) the determination of the drop and impact points, taking into account the quantity of regolith contained in the scoop, without disconnecting the tether by either stretching it or by moving the pin toward the lander (Golombek et al., 2023; Yana et al., 2023). Other issues were related to properly accounting for the direction and amplitude of the winds to plan the dump in an efficient way, without any excessive dispersion of the dumped regolith.

Replicas of the instruments of the InSight mission were used in test beds at both JPL and CNES. To properly dump the regolith onto the SEIS tether, the IDA group designed a sequence as follows: first, the scoop was moved above the tether as shown in (Figure 5); then, the scoop was rotated around the scoop tip, keeping the tip in the same location throughout the rotation, while the rest of the scoop had to be moved around it (Figure 7). To do so, the three IDA pitch joints had to be simultaneously mobilized. The first motion rotated the scoop until the back of the scoop was almost parallel to the lander deck. The second motion rotated the scoop until the back of the scoop was just past the lander deck plane. The third motion rotated the scoop along the remainder of the way until the scoop back was mostly vertical.

Using scoop replica and regolith simulant (Cannon et al., 2019) in the testbed (Figure 8), the dumping height had to be several tens of centimeters above the terrain (Table 3) to guarantee there would be no contact with the WTS and reduce wind dispersion during dumping (Lapeyre et al., 2022; Yana et al., 2023). For the two first dumps (sols 816 and 850) that were poured onto the top of the WTS, the scoop tip was placed 55 cm above the terrain. The remaining four dumps (sols 856, 863, 870, and 877, see Table 2) were no longer poured on the WTS. The scoop started the dumping close to the WTS, from a height of 45 cm above the terrain (Table 3).

A total of six dumps were performed before entering the winter season and stopping the arm activities. In order to monitor the operations by the cameras, dumps were first performed in the afternoon, during the least windy

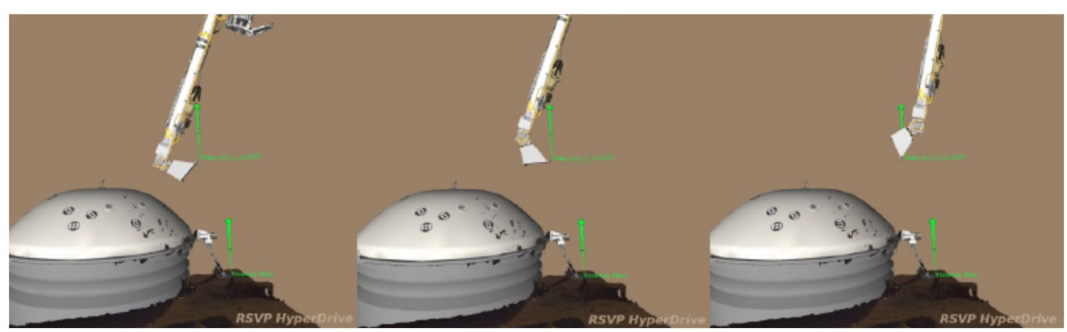


**Figure 7.** Simulated side view of the Instrument Deployment Arm and WTS, showing the scoop rotating around the dumping location while keeping the scoop tip in the same location. No images from Mars are available from the side due to the location of the cameras.

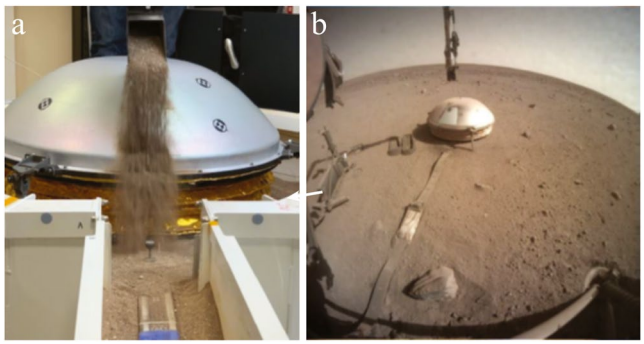


**Figure 8.** Dump performed taking advantage of the WTS curvature to guide the regolith as close as possible to the insulation skirt connecting the WTS with the soil. (a) Mimicking the dump on Earth on the CNES testbed (credit CNES). A qualification model of the WTS was used along with a 3D printed scoop. (b) Dumping on Mars: Instrument Context Camera picture taken on sol 816 from the lander (Credits NASA/JPL/CalTech). A lander foot can be seen at the bottom right corner. The tether goes from the bottom left to the center, where the WTS stands. At the top center of the image, a section of the robotic arm can be seen, with the scoop at its extremity. The picture was taken some seconds after the dump.

times of the Martian daytime (Banfield et al., 2020). As shown in various orthorectified photos taken by the IDC above the regolith piles (Figure 9), the tether was completely covered between the WTS (white area in the upper right corner of the images) and the pinning mass (blue circular contour line in the center of the images) by a 4 cm high pile of sand above the Martian ground with a basal surface of ∼334 $cm^2$. From the difference in DEMs before and after deposition, the mean volume of regolith deposited on the tether at each dump was around 55 $cm^3$ (Table 2), with a total amount of 389.0 ± 234.3 $cm^3$ at the end of the dump #6 (Figure 9).

### 2.4. Investigation of the Regolith Fraction Dispersed by Wind

Despite the relatively high spatial resolution of the IDC images (0.5 mm. $pixel^{-1}$), the grain size contained in the piles could not be precisely determined (Figure 9), except for a few very coarse sand grains (>1 mm), and granules with a diameter greater than 2 mm (Wentworth's classification, 1922), in good agreement with other data from the InSight landing site (Golombek, Warner, et al., 2020; Golombek, Williams, et al., 2020; Weitz et al., 2020). The shapes and slopes of piles have the same characteristics as a sand pile made of coarse sand (Marteau et al., 2022), suggesting a sandy grain size.

Surprisingly, a significant deficit between the volume of regolith extracted by shoveling and that deposited on the tether was observed. When comparing the total volume of regolith deposited (i.e., 389.0 ± 234.3 $cm^3$) and that contained in the scoops during shoveling (i.e., 652.5 ± 326.8 $cm^3$), we observe that about 40% of the material is missing, with no evidence of deposition beyond the piles on either the ICC and IDC images or the DEMs (Figures 2, 5 and 8–10). This discrepancy led the group to consider a possible effect of wind dispersion on the finer fraction of the dumped regolith.The localization of the plume made up of the fraction of regolith moved away by the wind from the pouring scoop and deposited was made possible by observing the wide-angle images provided by the ICC. Figure 10 illustrates such observations from sol 877 before (a) and after (b) dump #6, with a time period between both images of 10 min. Although no significant change between both images could apparently be detected, their subtraction and magnification following a method developed by Charalambous et al. (2021) clearly evidences the changes that occurred. As seen in Figure 10c, the dispersed regolith appears like a dark plume, longer than the 1.25 m observed in the figure. The plume starts close to the deposited sand pile and is oriented along the wind direction provided by the TWINS sensor, that is, coming from N140° (ESE) to N320° (WNW), with a mean wind speed of 5 $m.s^{-1}$. The widening shape of the plume along the wind direction is typical of aeolian plume deposits.

This method was used for all the dumps, but only dumps 3 to 6 were considered in this paper (Figure 11). The dark plumes show different sizes and elongation orientations, consistent with the various wind directions and

**Table 3**
*List of Dumps Performed and Their Associated Regolith Deposits*

| | | Acquisition and dump dates (in sols and LMST) | | | Pile summit distance to pinning mass along the tether (cm) | | |
|---|---|---|---|---|---|---|---|
| Pile name | Dump # | Acq | Dump | | Targeted | Achieved | Dump height (cm) |
| Aneto | 1 | 816 | 816 | 15:34 | N/A (indirect) | +6.90 | +55.00 |
| | 2 | 836 | 850 | 17:05 | N/A (indirect) | +6.90 | +55.00 |
| Canigo | 3 | 856 | 856 | 16:56 | +0.00 | +5.00 | +45.00 |
| Bastan | 4 | 863 | 863 | 16:46 | +0.00 | −0.50 | +45.00 |
| | 5 | 870 | 870 | 11:21 | +0.00 | +0.00 | +45.00 |
| Carlit | 6 | 877 | 877 | 11:30 | +5.00 | +5.00 | +45.00 |

*Note*. Name of pile, dump number, dumping date, horizontal distance between pinning mass and pile summit, height of scoop above the ground during dumping.

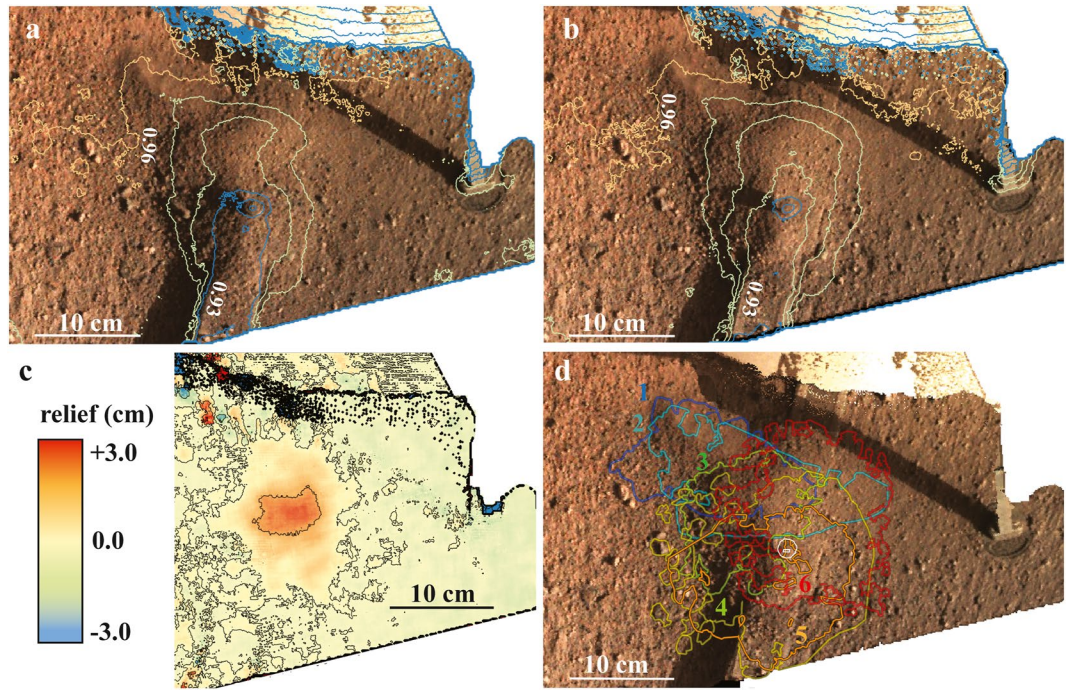


**Figure 9.** (a) Orthorectified image centered on pile #5 after dumping, sol 870. Color lines correspond to height contour lines with an interval of 1 cm. (b) Orthorectified image centered on pile #6 after dumping, sol 877. Note that the tether has been totally covered between the WTS (white area at the top of image) and the pin (circular blue contour line at the center of image) with regolith forming a 4 cm high sandy pile above the Martian ground. (c) Relief of sandy pile between sol 877 (dump 6) and sol 870 (dump 5). The interval of contour line is 1 cm. (d) Location of sandy deposit at different sols: 1. Sol 816 (blue contour line), 2. Sol 851 (blue green), 3. Sol 857 (green), 4. Sol 864 (green yellow), 5. Sol 870 (yellow) and 6. Sol 877 (red).

speeds recorded by the TWINS sensors. Note the curved shape of the plume of dump 4, showing the effect of the spheric shape of the WTS on the wind flow around it.

## 3. Grain Size Determination by Numerical Modeling and Simulations

Given that it was not possible to directly constrain the GSD of the scraped regolith by image analysis due to the insufficient resolution, it was found relevant to determine it by using the wind as a natural sorter. The principle of sorting the poured regolith particles submitted to wind is based on the fact that particles are simultaneously

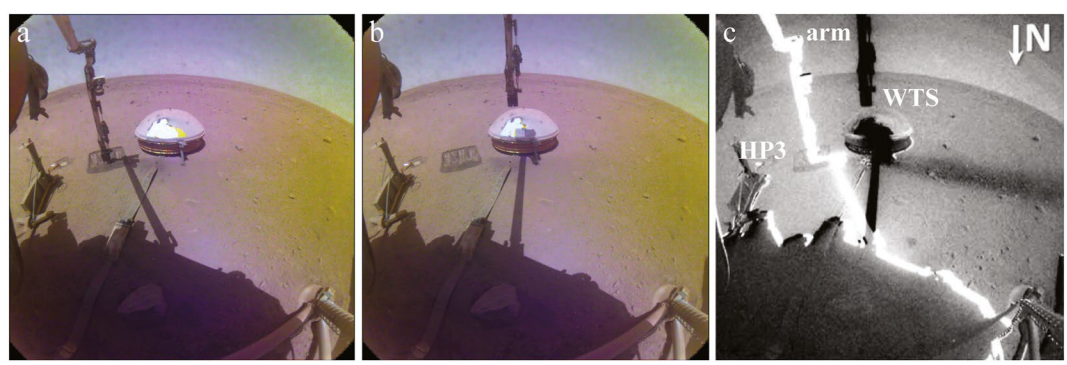


**Figure 10.** (a) Instrument Context Camera (ICC) image taken on sol 877 at 11:22 a.m. before dump 6. (b) ICC image acquired on sol 877 at 11:33 a.m., after dump 6. (c) ICC image difference showing the dark plume made up of wind dispersed and transported particles. The plume extends to the right from the WTS, and its orientation corresponds to the wind direction from N14° (ESE) to N320° (WNW).

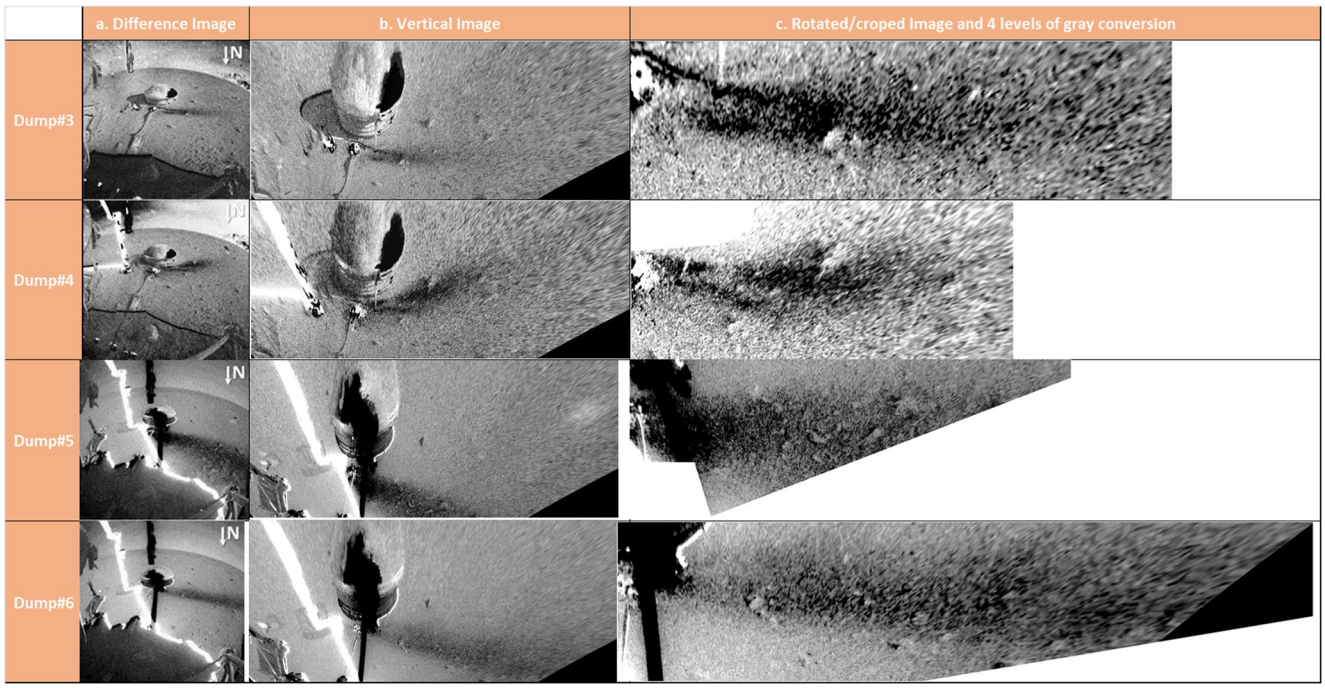


**Figure 11.** Image processing steps for the last four dumps, showing the dark plumes corresponding to particles dispersed and transported by the wind. The difference in orientation, shape and length of the plumes corresponds to different wind orientations and speeds. (a) Difference Images following a method developed by Charalambous et al. (2021) (b) Vertical images provided by the JPL-MIPL team (c) Image processing done by the author (see Section 3.1.3).

subjected to the effects of weight, buoyancy, and wind drag. As a consequence, finer and lighter particles will be transported and deposited further than larger and heavier ones. This physical consideration is the basis of the computational fluid mechanics models developed and implemented in this work.

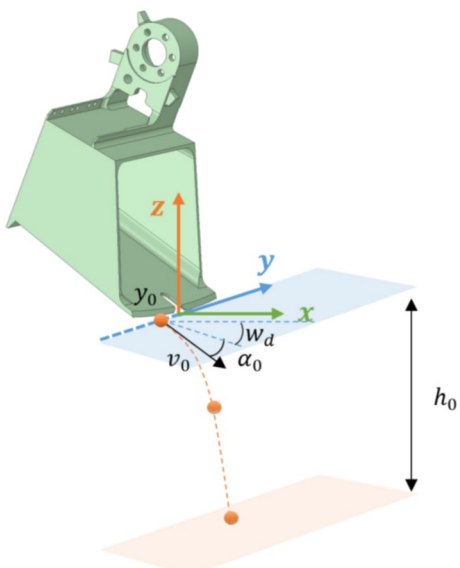


**Figure 12.** Initial geometric and kinematic conditions of the model defined by the height $h_0$ of the scoop above the ground, the position $y_0$ of the grain along the scoop tip, the initial grain velocity $v_0$ and the angle $\alpha_0$ of the grain trajectory relative to the vertical when the grain leaves the scoop.

In order to compute the trajectory and the distance at which the grains are settled on the Martian ground from the scoop, we have used two independent numerical modeling packages: the first model solves the first-order force equations using a multi-physics system modeling software called "Simulink" integrated in Matlab (Moler, 1980); the second one uses a comprehensive general purpose computational fluid dynamics (CFD) software package for engineering analysis and design optimization of enterprise applications, based on ENGYS' own open-source CFD simulation engine (ENGYS, 2022).

## 3.1. Methods

### 3.1.1. Basic Model for Grains Ballistic Range Estimation

#### *3.1.1.1. Theoretical Background*

The trajectory of a grain released by the scoop and submitted to wind is determined by different forces projected along 3 axis, with the vertical "$z$" axis aligned with the gravity vector (opposite direction), the "$x$" axis along the wind direction $w_d$ and the "$y$" axis along the tip of the scoop (Figure 12). The angular value between $x$ and $y$ axes hence depends on the wind direction.

Assuming no particle-particle interaction and no action from the particles on the fluid, and applying Newton's laws of motion for each (spherical) grain, we obtain

$$\rho_s \cdot V \cdot \frac{d\vec{v}}{dt} = \vec{P} + \vec{B} + \vec{F_w} + \vec{F_{\text{atm}}} \quad (1)$$

with $\overrightarrow{P}$ the weight of the particle, given by

$$\overrightarrow{P} = -\rho_s \cdot V \cdot g \cdot \vec{z} \tag{2}$$

where $g$ is the Martian gravitational acceleration (3.72 m.s$^{-2}$), $V$ is the grain volume (m$^3$) and $\rho_s$ the grain density (kg.m$^{-3}$). As Elysium Planitia is mainly composed of volcanic flows with probable basaltic composition from orbital imagery (Golombek, Warner, et al., 2020; Golombek, Williams, et al., 2020; Golombek et al., 2018; Viviano et al., 2019; Warner et al., 2022), the grain density of basalt ($\rho_s$ = 3,000 kg.m$^{-3}$) was used. For a spherical grain with a diameter $D$ (m), $\overrightarrow{P}$ is given by:

$$\overrightarrow{P} = -\frac{\rho_s \cdot \pi \cdot D^3 \cdot g}{6} \cdot \vec{z} \tag{3}$$

The buoyancy force $\overrightarrow{B}$ is derived from Archimedes theory defined as

$$\overrightarrow{B} = \rho_{\text{atm}} \cdot V \cdot g \cdot \vec{z} = \frac{\rho_{\text{atm}} \cdot \pi \cdot D^3 \cdot g}{6} \cdot \vec{z} \tag{4}$$

where $\rho_{\text{atm}}$ is the Martian atmospheric density (Mg.m$^{-3}$).

The drag forces $\overrightarrow{F_w}$ and $\overrightarrow{F_{\text{atm}}}$ due to the wind and atmospheric friction, respectively, are defined as

$$\overrightarrow{F_{\text{atm}}} = \begin{pmatrix} -\frac{\rho_{\text{atm}} \cdot C_d \cdot S \cdot {v_x}^2}{2} \\ -\frac{\rho_{\text{atm}} \cdot C_d \cdot S \cdot {v_y}^2}{2} \\ \frac{\rho_{\text{atm}} \cdot C_d \cdot S \cdot {v_z}^2}{2} \end{pmatrix} \begin{pmatrix} \vec{x} \\ \vec{y} \\ \vec{z} \end{pmatrix} = \begin{pmatrix} -\frac{\rho_{\text{atm}} \cdot C_d \cdot \pi \cdot D^2 \cdot {v_x}^2}{8} \\ -\frac{\rho_{\text{atm}} \cdot C_d \cdot \pi \cdot D^2 \cdot {v_y}^2}{8} \\ \frac{\rho_{\text{atm}} \cdot C_d \cdot \pi \cdot D^2 \cdot z^2}{8} \end{pmatrix} \begin{pmatrix} \vec{x} \\ \vec{y} \\ \vec{z} \end{pmatrix} \tag{5}$$

$$\overrightarrow{F_w} = \frac{\rho_{\text{atm}} \cdot C_d \cdot S \cdot w_s(z)^2}{2} \cdot \vec{x} = \frac{\rho_{\text{atm}} \cdot C_d \cdot \pi \cdot D^2 \cdot w_s(z)^2}{8} \cdot \vec{x} \tag{6}$$

where $S\left(=\frac{\pi \cdot D^2}{4}\right)$ is the reference area, $C_d$ the drag coefficient, $v_z$ the vertical particle speed and $w_s(z)$ the magnitude of the horizontal wind speed component.

Finally, the lift force is neglected here because the particles are considered spherical in the grain size range (i.e., 100–1,000 microns) of our model, in conjunction with the sub-rounded to rounded shapes of sand grains observed at the surface of Mars (e.g., Goetz et al., 2010 in the Phoenix landing site); so, at low Reynolds number $R_e$ as in the Martian conditions due to atmospheric pressure, temperature, and density, the flow is stationary.

Given that Equation 1, which can be rewritten as a differential equation for particle velocity, is nonlinear, a Matlab Simulink model was developed to solve it using the projected equation derived from Equation 1 as follows:

$$\frac{dv_z}{dt} = \left(\frac{\rho_{\text{atm}}}{\rho_s} - 1\right) \cdot g + \frac{3}{4} \cdot \frac{\rho_{\text{atm}}}{\rho_s} \cdot \frac{C_d}{D} \cdot {v_z}^2 \tag{7}$$

$$\frac{dv_x}{dt} = \frac{3}{4} \cdot \frac{\rho_{\text{atm}}}{\rho_s} \cdot \frac{C_d}{D} \cdot \left(w_s(z)^2 - {v_x}^2\right) \tag{8}$$

$$\frac{dv_y}{dt} = -\frac{3}{4} \cdot \frac{\rho_{\text{atm}}}{\rho_s} \cdot \frac{C_d}{D} \cdot {v_y}^2 \tag{9}$$

By integrating Equations 7–9, the position of the grain can be known until reaching the final condition $z = 0$, that ends the simulation of the trajectory.

#### *3.1.1.2. Determination of the Parameters*

The density of Mars' atmosphere $\rho_{\text{atm}}$ can be calculated by using the meteorological data provided by the on-deck mounted Auxiliary Payload Sensor Suite (APSS) instruments (Banfield et al., 2019) when the dumps occurred. According to the ideal gas law, it depends on the local pressure $P_a$ and temperature $T_a$ of the Mars atmosphere:

$$\rho_{\text{atm}} = \frac{P_a \cdot M_a}{R \cdot T_a} \tag{10}$$

in which $R$ is the ideal gas constant (8.314 J.K$^{-1}$.mol$^{-1}$). The molar mass of the atmosphere, $M_a = 43.35$ g.mol$^{-1}$ can be directly calculated assuming a Martian atmosphere made up of 95.1% carbon dioxide, 1.9% argon and 2.6% nitrogen (Trainer et al., 2019).

The wind velocity and direction given by the TWINS sensors were averaged over the dump duration, while the standard deviation feeds the error budget. Because the wind is measured on the lander at 1.2 m above the ground, a logarithmic correction is applied, as described by Spiga et al. (2018), with the following expression for vertical profile of the magnitude of the horizontal component of the wind:

$$w_s(h) = w_0 \frac{\ln\left(\frac{h}{r}\right)}{\ln\left(\frac{h_s}{r}\right)} \tag{11}$$

where $h$ is height above ground, $w_0$ is the wind speed measured by the TWINS sensors at $h_s = 1.2$ m above the ground and $r$ the surface roughness. This parameter has been estimated by Charalambous et al. (2021) at the Insight landing site, with $r = 1$ cm.

In a neutral atmosphere, the drag coefficient of a sphere $C_d$ mainly depends on the density and viscosity of the fluid and varies widely depending on the Reynolds number $R_e$ defined by

$$R_e = \frac{v \cdot D \cdot \rho_{\text{atm}}}{\mu(T)} \tag{12}$$

Where $v$ is the velocity measured in the direction of motion, $\mu(T)$ is the dynamic viscosity of the Mars atmosphere, defined by Sutherland's law (Sutherland, 1893):

$$\mu(T) = \mu_0 \frac{T_0 + \Upsilon}{T_a + \Upsilon} \left(\frac{T_a}{T_0}\right)^{\frac{3}{2}} \tag{13}$$

where $T_0 = 273$ K, $\Upsilon = 222$ K is independent of temperature, being determined only by the parameters of the intermolecular attraction (Chapman & Cowling, 1970), and $\mu_0$ is the dynamic viscosity at $T_0$, with $\mu_0 = 1.37 \times 10^{-5}$ N.s. m$^{-2}$.

Considering the pressure, temperature, and density encountered on the surface of Mars, the Reynolds number remains below 10. For such a low number, the drag coefficient of the sphere can be expressed according to Stokes' Law (1845):

$$C_d = \frac{24}{R_e} \tag{14}$$

yielding:

$$C_d = \frac{24 \cdot \mu(T)}{v \cdot D \cdot \rho_{\text{atm}}} \tag{15}$$

The drag coefficient from Equation 15 is substituted into Equations 4 and 5.

**Table 4**
*Initial Constant Parameters for Simulations*

| | Dumps | | |
|---|---|---|---|
| Parameters | Value | Accuracy | Variability |
| Soil roughness (cm) | **1** | −0,07 | – |
| Gravity (m/s$^2$) | **3,72** | – | – |
| Particle density (kg/dm3) | **3** | – | ±0.2 |
| Release height (cm) | **45** | ±1.5 | – |
| Initial velocity (m/s) | **0,15** | ±0.07 | – |
| Atmosphere molar mass (g/mol) | **43,34** | – | – |

#### 3.1.1.3. Initial Conditions

The initial geometric and kinematic conditions of the model are defined by the height $h_0$ of the scoop above the ground, the position $y_0$ of the grain along the scoop tip, the initial grain velocity $v_0$ and the angle $\alpha_0$ of the grain trajectory relative to the vertical when the grain leaves the scoop (Figure 12). The position $y_0$ of the grain is arbitrarily defined by the simulator within a range of 7 cm corresponding to the scoop width. Table 4 shows the initial parameters used for all dumps.

The precise estimation of the grain initial velocity $v_0$ is challenging. It is controlled by the friction angle of the regolith and results from the mutual sliding of the grains at the surface of regolith contained in the scoop when

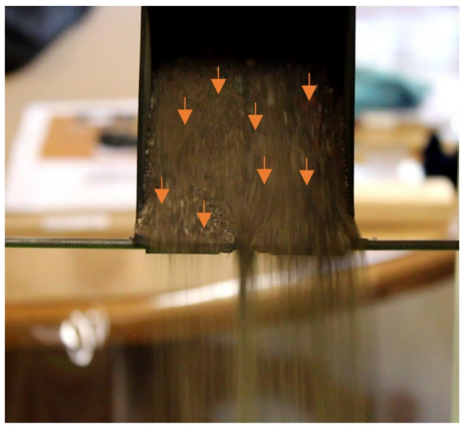

**Figure 13.** A dump of regolith simulant is performed on Earth (CNES lab) with an Insight 3D printed scoop. Up to 10 regolith colored grains were identified in the movie and their velocity determined. By repeating the test various times, a mean speed value was calculated together with the corresponding standard deviation.

a critical inclination of the regolith slope triggers the slope instability at the surface. It was determined on Earth by measuring the speed of many surface grains of a Martian regolith simulant within the scoop using a camera when the critical inclination was reached and instability triggered (Figure 13). Ten colored grains were identified in the movie and their velocity determined. By repeating the test multiple times, a mean speed value of 0.15 $m.s^{-1}$ was calculated together with the corresponding standard deviation. Note that a large error bar of ±50% was applied to this parameter. Given that this phenomenon is mainly governed by the friction angle, the same value was adopted in Mars conditions.

The angle of ejection $\alpha_0$ is derived from correlating the arm motion (monitored through the change in wrist angle with time) and the seismic data (Mars SEIS data service, 2019) monitored by the SP seismometer during dumping. As shown in Figure 14, that presents both data together, the seismic signal is not continuous, suggesting a regolith deposit by successive impacts of the grains. The signal is however clear enough to estimate with good accuracy the start and end times of the regolith dumping and impact on the surface, that occurred between 16:47:16.500 and 16:47:21.000, (i.e., a duration of 4.5 s for dump #4, see Figure 14). The signal also enables the determination of related angle $\alpha_0$ of scoop tilt: the scoop tilt relative to the horizontal plane was −21.3° at the beginning of dumping and reaching −35.7° at the end of dumping (see Figure 14). Because this value is done in the local arm frame, additional calculations are necessary to express the angle $\alpha_0$ relative to the horizontal plane.

#### *3.1.1.4. Simulations*

We used the numerical solver Simulink™ integrated in Matlab™ to solve Equations 7 to 9 because (a) these equations are not linear, and (b) to take into account the initial conditions on Mars (Section 3.1.1.3). Simulink is a block diagram environment used to design systems with multidomain models, to simulate before moving to hardware, and to deploy without writing any code. The simulation is launched automatically by a Matlab script for each grain and stopped when the grain reaches the floor. The main outputs of the simulation are the coordinates of grain impacts on the floor in the scoop frame (Figure 15). In addition, the ballistic range of the grain, that is,

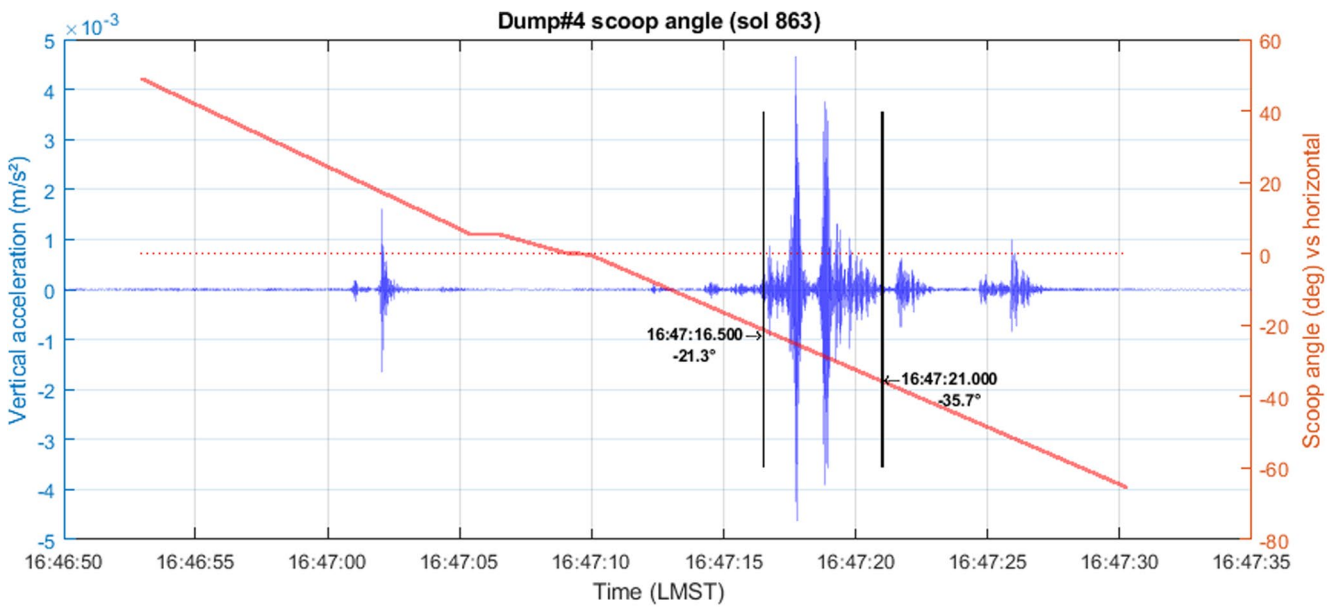


**Figure 14.** Superimposition of the seismic signal measured by the SP seismometer for dump #4 with the extrapolated scoop angle versus horizontal. The start and stop time of the regolith impact can be extrapolated by considering the calculated fall time of the particles, so as to give the related scoop angular values.

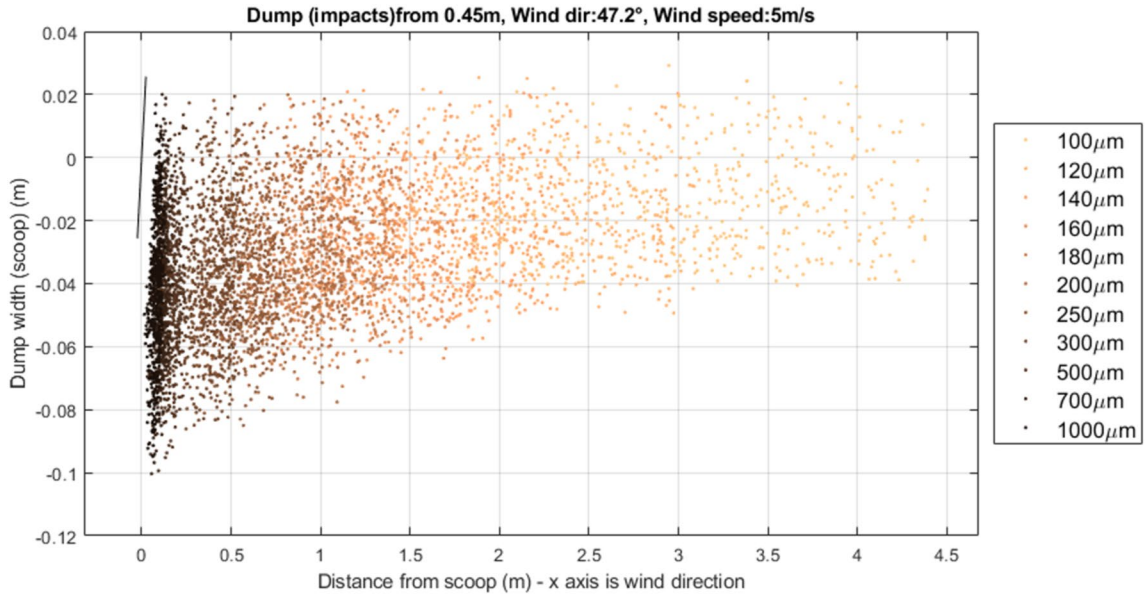


**Figure 15.** Simulation output for dump 6, the impacts of the 5,500 grains (500 grains for each 11 size mentioned in the legend) are represented. The color of each grain depends on its size in the 100–1000 μm range. The *x* axis is in the mean wind direction, and the scoop is the small black line (top left).

the horizontal distance of the impact relative to the scoop can be reported (Figure 16) with error bars taking into account the variability and accuracy of the input parameters. These error bars are useful to determine the optimal size classes. Note that grains coarser than 500 μm fall near the pouring zone and are not carried away by the wind.

### 3.1.2. CFD Simulation for Grains Ballistic Range Estimation

In parallel to the modeling with Simulink, the CFD solver HELYX was used with the aim to consolidate, by using a second method, the relation between size and ballistic impact of grains. The HELYX solver encompasses a Lagrangian particle tracking approach (Amsden et al., 1989; Gousbet & Berlemont, 1999; Nordin, 2001), which

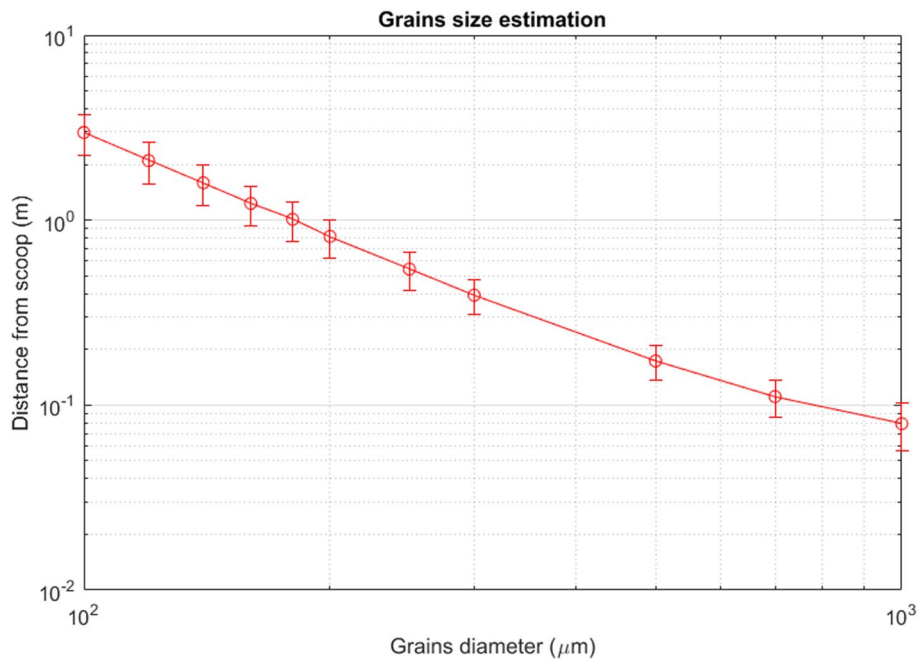


**Figure 16.** Distance from scoop versus grains and settled diameters for dump 6.

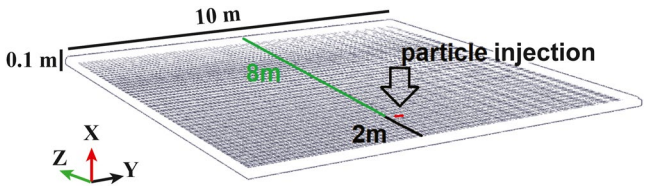


**Figure 17.** Mesh and position of the particle injection into the domain (scoop position).

is perfectly suited to model the trajectory of the grains in a fluid. The equations used to model the grain trajectory are presented below:

$$\begin{cases} \nabla \cdot U = 0 \\ \frac{\partial U}{\partial t} + \nabla(U \cdot U) - (\mu + \mu_t)\Delta U + \nabla Pa = 0 \\ \rho_s \frac{dU_p}{dt} = \frac{1}{V_p} \sum F_i \\ U_p = \frac{dX_p}{dt} \end{cases} \quad (16)$$

With:

- $U_p$: particle velocity
- $U$: fluid velocity
- $Pa$: fluid pressure
- $X_p$: position of the particle
- $\mu_t$: turbulent dynamic viscosity
- $\sum F_i$: Sum of forces applied to the particles including drag, gravity and buoyancy forces

All parameters and initial conditions are similar to those used in the Simulink solver.

The CFD simulation consists in solving Equation 16 for up to 100,000 grains distributed along a large size range from 1 mm to 1 µm. It significantly increases the number of modeled particles compared to that injected in Simulink (i.e., 5,500 grains). The CFD simulation is a 1-way coupling equation of the Eulerian-Lagrangian part, since only the force from the fluid acting on the particles is modeled. The particles are injected into the fluid domain by a source term in equation [16] through a 7 cm × 3 cm surface corresponding to the scoop size and a variability of ±1.5 cm on the release height (45 cm). The 3D mesh is composed 50 × 200 × 200 cells, corresponding to a volume of [0.1 m; 10 m; 10 m], in which the $X$ axis is oriented along the height of the 3D mesh (Figure 17).

The main outputs of the CFD simulation are the coordinates of grain impacts on the ground, which are compared to those observed on the vertically projected differentiated ICC image. In addition, the ballistic range of the grains (i.e., the distance of the impact relative to the scoop) can be reported with a distribution taking into account the variability and accuracy of input parameters.

### 3.1.3. Volume Estimations

Additional simulations were performed to estimate the spatial distribution of grains transported by the wind and deposited downwind with a distance from the scoop linked to their diameters. Starting from the subtracted ICC images before and after the dump (Figure 11a), a vertical projection was performed on each image at the Multi-mission Instrument Processing Laboratory of JPL (Figure 11b) with a pixel of 1 mm × 1 mm. On each image, one can infer a mean axis on each plume that corresponds to the wind direction and will correspond to the $x$-axis in the modeling. The images are rotated with their axis parallel to horizontal and carefully cropped to include all the dispersed material. Finally, all images are converted in 4 Gy level bitmap and optimized to enhance the contrast and to compensate different light expositions due to the different acquisition dates (Figure 11c). In the first approach, the two lower gray levels are considered without grains, the third as a thin layer filled at 50% by dispersed regolith and the upper like a full layer (in black). This approach refines the estimation compared to a binary image.

The next step consists of defining areas on the images which contain the portion of regolith for each size range (Figure 18). The class boundaries for the final histogram are selected in such a manner that all classes don't have necessarily the same width. Thus, the left and right edges of the sub-images correspond to the upper and lower sizes of grains, respectively, for a given class. The number of sub-images is the number of classes for the granulometry histogram. Some images include the shadows of the SEIS or tether, which jeopardizes the individual grain density estimation. As a result, the sub-image images do not start necessarily at the left border of the main one, somewhat compromising the estimation of large grains.

Because each pixel is larger than most of the grains, it is not possible to count them individually. Nevertheless, a pixel $x$ meters away from the scoop represents a volume $V_p(x)$ of dispersed regolith, given by:

$$V_p(x_p) = d(x_p) \cdot \eta_p \cdot S_p \quad (17)$$

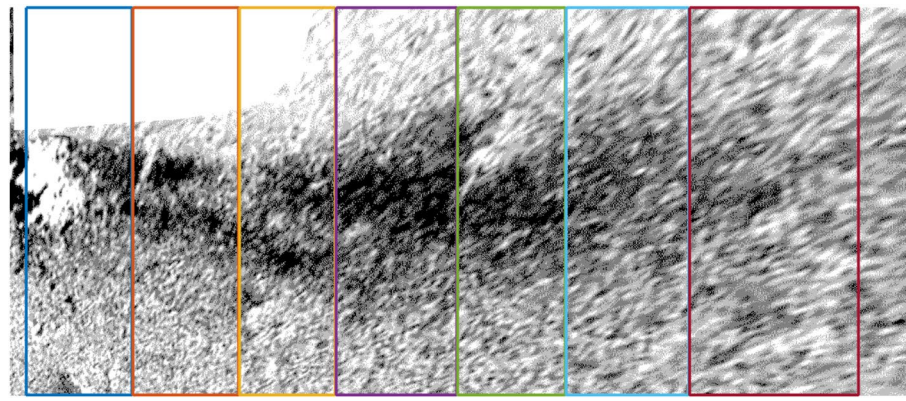

**Figure 18.** Instrument Context Camera image of dump #4 vertically projected on which seven sub-images (color boxes) have been plotted. The dark blue box on the left side includes the larger grains, while the brown one on the right side captures the smallest ones. The scoop is at the left image border. The size range of grains in each box is defined by the left and right border distance from the scoop.

where $d(x)$ is the diameter of grains given by the model (Section 3.1.1.4) at $x$ meters from the scoop, $S_p$ the surface of the pixel (1 mm$^2$) and $\eta_p$ the filling coefficient (1 for a dark pixel, 0.5 for a gray pixel, 0 for white or light gray pixel).

For a given area $i$, the volume of dispersed material $V_{a_i}$ is:

$$V_{a_i} = \sum_n d(x_p) \cdot \eta_p \cdot S_p \tag{18}$$

Where $n$ represents all the pixels $p$ in the area $i$.

Considering all areas, the volume of dispersed material defined for each dump using DEM (Section 2.2 and Table 2) should be retrieved by summation of all areas. Unfortunately, this proved challenging for various reasons. First, because an unknown volume $V_0$ of fine grains are likely to be dispersed in the Mars atmosphere; second, because the plume is too large to be fully captured by the ICC camera (see dumps #5 and #6 for instance, Figure 11); third, because the volume estimation $V_{a_i}$ of each area is sensitive to the image contrast.

Nevertheless, if this sensitivity affects the total volume restitution $V_d$, the relative dispersed volume between areas remains relevant with respect to the GSD, with an error equals to $V_0$ divided by $V_d$, where

$$V_d = V_0 + \sum_{i=1}^{m} V_{a_i} \tag{19}$$

with a relative ratio $r_i$ for each class $i$ among $m$ equals to:

$$r_i = \frac{V_{a_i}}{V_d} \tag{20}$$

The last step consists of relating the distance from the scoop to the grain size in order to obtain the relative ratio for each size class. Finally, this relation size-vs.-distance relationship, associated with Equation 17, allows us to propose the GSD of Mars regolith at the InSight landing site.

### 3.2. Results

Here, we present the grain sizes and their spatial distribution on the ground near the InSight WTS, deduced from numerical simulations, taking into account the Martian atmospheric conditions prevailing during the four scoop dumps.

#### 3.2.1. Comparison Between Matlab-Simulink Basic Model and CFD Simulations

The main output of the CFD simulations is the map of grain impact locations on the ground superimposed on the vertically projected differentiated ICC image (Figure 19). We observed a good correlation between the

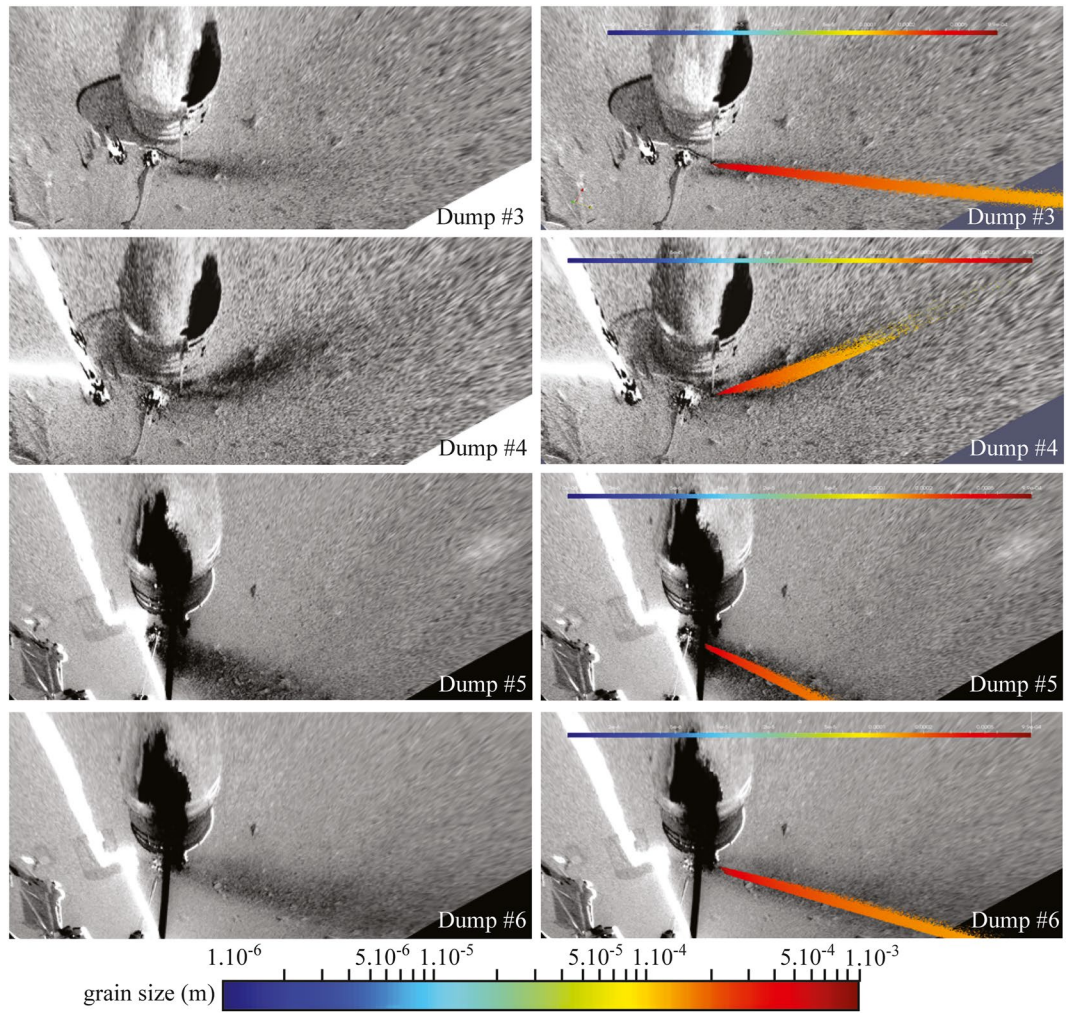


**Figure 19.** The grain size distribution projected on vertically projected differentiated Instrument Context Camera (ICC) images during different dumps using computational fluid dynamic simulations. The left column shows the ICC images and the right column shows 100,000 grains plotted on the ICC images with the color corresponding to the grain size ranging from 1 micron (blue) to 1 mm (red).

direction of the main deposit area and the wind direction for each dump. A small discrepancy between the width of the deposited grain areas observed on the ICC images and that computed by the CFD model is observed. This discrepancy is likely due to the 1-way coupling approximation (i.e., no particle-particle interaction or no action from the particles on the fluid is taken into account in the simulation). As observed in the Simulink simulation, the distribution of grains on the ground shows a decrease in grain size with distance from the pouring point, with a size ranging from 1 mm near the dump point to ∼100 μm in the farthest area observed in the ICC images (Figure 19).

In addition, the ballistic range of the grains (i.e., the distance of the impact relative to the scoop) is plotted as a function of their size (Figure 20). The CFD simulation performs a random draw in the ranges of variations of input parameters (Tables 2, 4, and 5) and on the grain size for 100,000 grains. The result is a point cloud on the grain size range curve. For each grain size, a probability density function (pdf) is visualized as the number of points in the vicinity. The maximum of the distribution is then compared with the same initial conditions as the Matlab Simulink model (black line in Figure 20) for the whole size range.

For all dumps, we observe that the Matlab model gives results close to the CFD model, with Matlab curves remaining within the probability distribution of the CFD model, which is satisfactory and provides some confidence in both approaches. This is particularly true within the 100–500 μm range. Beyond this range, we observe

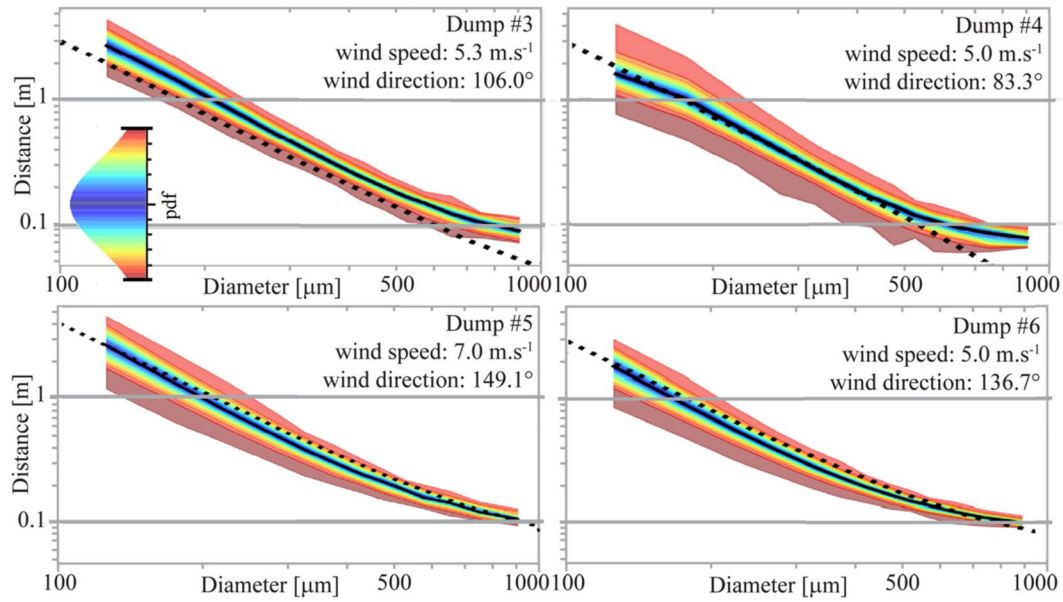


**Figure 20.** Distance from scoop versus grain size for each dump, with the probability density function (pdf) associated with the computational fluid dynamics (CFD) simulation, compared to the calculated curve from the Matlab model. The dark blue line is the mean curve obtained by CFD simulation. Dashed lines represent the mean distribution curves obtained by the Simulink model.

a small divergence of the models, which can be explained by a greater sensitivity of the ballistic range to the initial conditions. Indeed, for the heaviest particles, the wind has little effect, whereas the speed and direction of the grains at the time of release are decisive. However, this has no impact on the overall study since these grains within the 500 µm-1 mm range are not carried downwind.

In summary, as expected, grains are transported further away in relation to their smaller size in windy conditions. Based on these four dumps, the numerical simulations enable to better constrain the GSD of the Martian regolith at the InSight landing site: Grain sizes range from coarse sand (900 µm) to fine sand (i.e., 115 µm) with, however, possible content of smaller particles blown away by the wind and not quantifiable with the available data.

**Table 5**
*Initial Simulation Parameters for the Dumps #3 and #4*

| | Dump #3 16:57:19.5 to 16:57:32 LMST | | | Dump #4 16:47:16.5 to 16:47:21 LMST | | |
|---|---|---|---|---|---|---|
| Parameters | Value | Accuracy | Variability | Value | Accuracy | Variability |
| Wind direction (°) -TWINS | **106,6** | ±22.5 | ±18.9 | **83,3** | ±22.5 | ±2.5 |
| Wind direction (°)—vertical projection | **94** | −5 | | **75** | −5 | |
| Wind speed (m/s @ 1.2 m above ground) | **5,3** | 1 | ±1.1 | **5** | 1 | ±0.1 |
| Temperature (K) | **227** | 5 | – | **228,3** | 5 | – |
| Pressure (hPa) | **7,2** | – | – | **7,2** | – | – |
| Soil roughness (cm) | **1** | −0,07 | – | **1** | −0.07 | – |
| Gravity (m/s$^2$) | **3,72** | – | – | **3,72** | – | – |
| Particle density (kg/dm3) | **3** | – | ±0.2 | **3** | – | ±0.2 |
| Release angle (°) | **−11.2 to −51.3** | −1 | – | **−21.3 to −35.7** | −1 | – |
| Release height (cm) | **45** | ±1.5 | – | **45** | ±1.5 | – |
| Initial velocity (m/s) | **0,15** | ±0.07 | – | **0,15** | ±0.07 | – |
| Atmosphere molar mass (g/mol) | **43,34** | – | – | **43,34** | – | – |

*Note*. "Wind Direction—Vertical Projection" Is the Value of Wind Direction Assessed by Measuring Plume Mean Direction on the Vertical Images

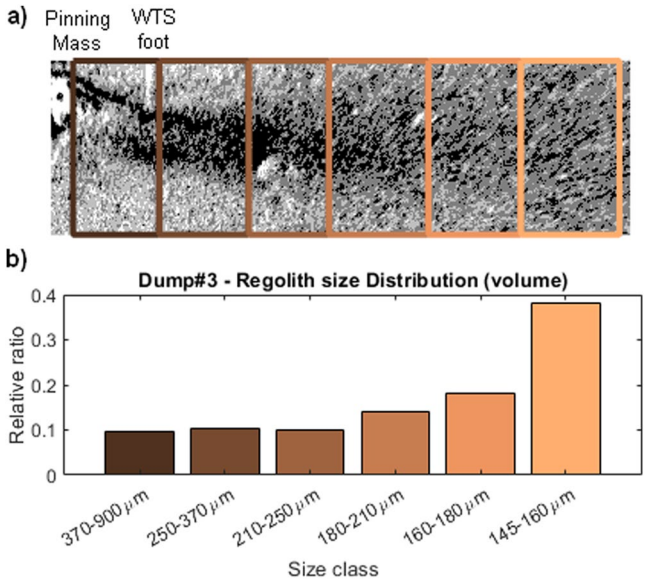


**Figure 21.** The grain size distribution for dump #3 was obtained using Matlab Simulink. (a) Spatial distribution of grain size along the plume direction (picture width represents 1.53 m). Wind speed is 5.3 m.s$^{-1}$ The color of boxes is directly correlated to the grain size viewed in (b) (b) Volume frequency versus grain size.

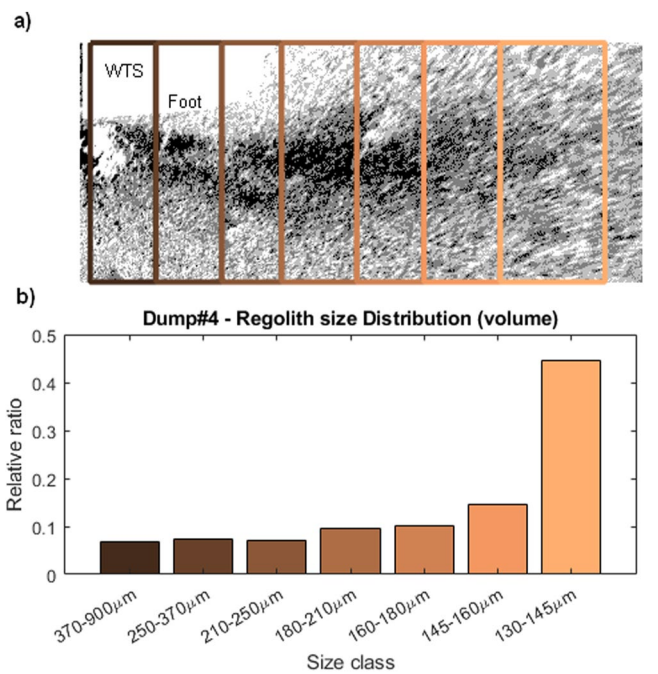


**Figure 22.** The grain size distribution for dump #4. The same legend as Figure 20, picture width represents 1.9 m. Wind speed is 5 m.s$^{-1}$.

The Matlab Simulink method, that can be carried out on a standard desk computer, is more cost-effective than the CFD approach. The calculation time of the trajectories of the 5,500 grains (11 runs of 500 grains each) lasts 45 min on an Intel I7-6500@2.5GHz, 8 GB RAM, while the CFD model, that simultaneously calculates the trajectories of 100,000 particles of size between 100 and 1,000 microns, runs during 2.5 hr using a 2x AMD EPYC 7351, 16 × 8 GB DDR4 2666 MHz computer with 32 cores. Because the results are comparable, the results of Matlab Simulink simulation were less consuming and were used to feed the granulometry estimation process.

### 3.2.2. Volume Estimation of Regolith Deviated by Wind

The initial conditions of dumps #3 and #4 are close (Table 5) with a release height of 45 cm and a relatively low wind speed of 5 m.s$^{-1}$, almost constant during pouring (wind was measured by the TWINS instrument located at 1.2 m height at a horizontal distance of 1.5 m from the scoop). However, the release angle for dump #4 is smaller (i.e., −21.3° compared to −11.2° for dump #3) and the wind orientation differs by 23°, with a dominant direction coming from the East to the West (Table 5, Figures 20 and 21). Note also the high variability of wind directions for dump #3 (18.9 compared to 2.5° for Dump #4), probably due to a wind gust.

The extent of wind blow deposits can be seen in their entirety in the most differential ICC images (Figure 11), with an elongated plume along the wind direction. The plume length is about 1.5 m, with maximum widths of 0.15 m for dump #3 and 0.5 m for dump #4. The detailed view of the plume on the vertically projected differential ICC image for dump #3 (Figure 21a) shows that the plume splits into two branches near the WTS. This could be due to changes in wind direction during the dumping or due to the presence of eddies behind the pinning mass and the WTS.

As previously discussed, the vertically projected differential ICC images (Figures 11, 21, and 22) introduce some distortions, especially at the edges of the images. For dump #3 (Figure 21), the left side of the image is excluded from the analysis because of the brightness of the tether field joint. The right side is also excluded because of the strong distortion of the pixels, leading to an erroneous increase in the size of the deposited grains. Using the numerical simulation, six deposit areas are defined as a function of the grain size, ranging from 145 μm (right side of image) and 900 μm (left side), that is, sand size.

The volume distribution (Figure 21b) shows that 30% of wind-blown grains are greater than 210 μm along a distance of 0.6 m from the dump impact, with the same volume in the three boxes. The next 0.25 m farther away account for 15% of the volume of blown grains, with a size ranging from 180 to 210 μm. Beyond this distance, 55% of the volume of blown grains is composed of grains greater than 145 μm (i.e., fine sand). Note that the accuracy of the grain size is less in the furthest downwind, due to the distortion of pixel size. In any case, the majority of the wind-transported grains detected in the differential ICC image are of the size of sand particles.

For dump #4 (Figure 22), the shape of the plume is quite similar to that of dump #3, with two branches due to the relief of both the pinning mass and the WTS foot, that act as obstacles. The directions of the branches slightly deviate from the dominant wind direction (i.e., from ENE to WSW) beyond a distance of 1.5 m for the south branch, and of 0.7 m for the north one (Figures 11 and 22a). The grain size ranges from 130 to 900 μm, with good accuracy for grains smaller than 450 μm due to WTS and its shadow, on the left side of the projected differentiated ICC image. The volume distribution

**Table 6**
*Initial Simulation Parameters for the Dumps #5 and #6*

| | Dump #5 11:22:03.5 to 11:22:09 LMST | | | Dump #6 11:30:34.1 to 11:30:35.9 LMST | | |
|---|---|---|---|---|---|---|
| Parameters | Value | Accuracy | Variability | Value | Accuracy | Variability |
| Wind direction (°) -TWINS | **149,1** | ±22.5 | ±16.4 | **136,7** | ±22.5 | ±3.8 |
| Wind direction (°)—vertical projection | **121** | −5 | – | **103** | −5 | – |
| Wind speed (m/s @ 1.2 m above ground) | **7** | 1 | −1 | **5** | 1 | ±0.6 |
| Temperature (K) | **232,5** | 5 | – | **237,6** | 5 | – |
| Pressure (hPa) | **7,3** | – | – | **7,3** | – | – |
| Soil roughness (cm) | **1** | −0.07 | – | **1** | −0.07 | – |
| Gravity ($m/s^2$) | **3,72** | – | – | **3.72** | – | – |
| Particle density (kg/dm3) | **3** | – | ±0.2 | **3** | – | ±0.2 |
| Release angle (°) | **−26.6 to −40.8** | −1 | – | **−19.9 to −25.7** | −1 | – |
| Release height (cm) | **45** | ±1.5 | – | **45** | ±1.5 | – |
| Initial velocity (m/s) | **0,15** | ±0.07 | – | **0,15** | ±0.07 | – |
| Atmosphere molar mass (g/mol) | **43,34** | – | – | **43,34** | – | – |

*Note*. "Wind Direction—Vertical Projection" Is the Value of Wind Direction Assessed by Measuring Plume Mean Direction on the Vertical Images.

of grain size is quite similar to that of dump #4 for coarser grains, with 35% of grains greater than 180 µm, 10% of grains ranging from 180 to 210 µm. However, the volume ratio drops to 15% for 145–160 µm grains, instead of 38% for dump #3. 45% in volume of wind-blown grains are composed of fine sand ranging from 130 to 145 µm.

For the next two dumps, the initial conditions were similar (Table 6), to a slightly higher wind speed for dump #5 (i.e., 7 $m.s^{-1}$) and different wind directions, coming from SE toward NW, with low variability during the dumps. Despite the presence of the WTS, the dispersion of the grains by the wind does not seem to be disturbed, leaving a long SE-NW trending plume whose tip is not imaged by the ICC camera (Figure 11).

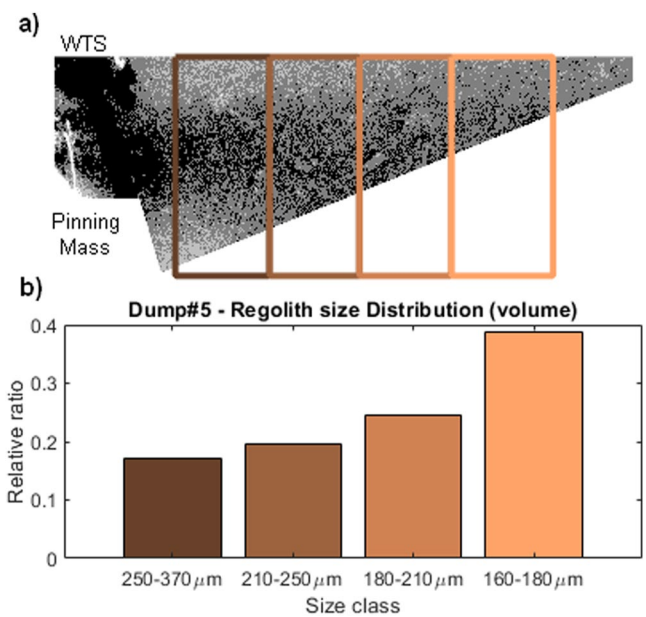


**Figure 23.** Grain size distribution for dump #5. Same legend as Figure 20, picture width represents 1.95 m. Wind speed is 7 $m.s^{-1}$.

For dump #5, the vertically projected differentiated ICC image only shows the area closest to the deposit, due to the FOV of the ICC camera (Figure 23). This alters the determination of the spatial distribution of grain sizes. In addition, the shadow of the robotic arm results in having an area excluded in the determination of grain size. Despite this, the grain size determination is better constrained between 160 and 370 µm, due to the very low pixel distortion in the projected ICC image (Figure 23). Almost 60% of the volume is composed of grains greater than 180 µm, which is twice higher than the volume ratio determined for dumps #3 and #4 for the same size range. 40% of the volume is composed of grains ranging from 160 to 180 µm, which is four times higher than those estimated for dumps #3 and #4. This increase in volume ratio for smaller grain class seems to show a spatial heterogeneity in the granulometric distribution of the surficial regolith near the SEIS instrument.

During dump #6, the atmospheric conditions were more favorable to image a large part of the grain deposit (Figure 11) with a lower wind speed (5 $m.s^{-1}$) oriented SW-NE (Table 6). The vertically projected differentiated ICC image covers the deposit with great accuracy, except near the SEIS seismometer, where the shadows of the IDA and WTS prevent the determination of GSD (Figure 24). Thanks to the elongated and narrow shape of the deposit, a better determination of grain sizes is possible, ranging from 110 to 400 µm. ~35% in volume of deposited grains are composed of grains greater than 160 µm. The next third of volume is made up of grains ranging from 132 to 160 µm. The last third of the volume is composed of very fine sand, with sizes between 115 and 122 µm. The grain size is probably much smaller further

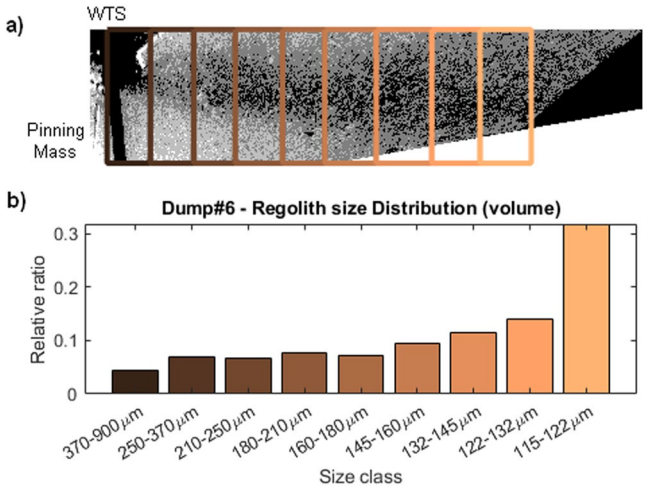


**Figure 24.** The grain size distribution for dump #6. The same legend as Figure 20, picture width represents 2.9 m. Wind speed is 5.3 m.s$^{-1}$.

away northwestwards, but unfortunately could not be estimated because of the limit of the ICC FOV.

## 4. Discussion

Significant wind sorting is inferred during the regolith pouring sequence of the SEIS tether covering operation, with a significant proportion (around 40%) of smallest particles blown away by the wind, whereas only 60% of the poured regolith was deposited on piles above the tether. Since wind data were accurately monitored by the TWINS sensors, the tether covering process provided a unique opportunity to further constrain the grain size distribution (GSD) of the poured regolith thanks to wind sorting, with smaller particles deposited further away from the tether. The length of the plumes of transported and deposited particles, observed from image analysis, is comprised between 1, 5 and 3 m, with wind speeds between 5 and 7 m.s$^{-1}$.

The two models used provided comparable data. Four GSD curves were derived with the MS model from dumps 3 to 6, with smallest particles having diameters between 115 µm (dump 6) and 145 µm (dump 3). Both calculations showed that, intuitively, smallest particles were deposited further away with stronger wind, at distances between 2 and 3 m. Extrapolating the Matlab Simulink data of Figure 20 shows that 100 µm diameter particles would be deposited at 3 m under 5 m.s$^{-1}$ and 5 m under 7 m.s$^{-1}$. These results support the hypothesis that fine sand can be driven by low velocity wind on Mars when the grains are already detached from the ground and blown off (e.g., Andreotti et al., 2021; Kok, 2010; Sullivan & Kok, 2017).

On Mars, we find such fine sand grains in the aeolian bedforms (dunes, ripples, sand sheets…) like those measured by the various instruments on board Mars rovers (e.g., Ehlmann et al., 2017; Lapotre & Rampe, 2018; Weitz et al., 2018, 2022) showed that they have been mobilized by the wind. These results also show that some of the regolith at the InSight landing site is from wind-borne grains trapped in the landing depression. In the vicinity of the InSight landing site, no dune fields are observed but only a few isolated bedforms are observed (e.g., Golombek, Warner, et al., 2020; Golombek, Williams, et al., 2020; Warner et al., 2022). However, in the InSight landing region, wind directions vary throughout the Martian year (Spiga et al., 2018, 2021; Banfield et al., 2019) and may carry sand either from northern martian plains or Nepenthes Mensae and Aeolis Planum composed of the Medusae Fossae formation, interpreted as fluvio-volcanic fine grained material (e.g., Kerber et al., 2011; Lefort et al., 2012; Mandt et al., 2008; Scott & Tanaka, 1986; Zimbelman et Griffin, 2010), characterized by pervasive fields of yardangs (wind-scoured hills; Boyd, 2018; Ward, 1979) indicative of easily friable material (Kerber et al., 2012) and dunes (e.g., Boyd, 2018; Burr et al., 2012; Hayward et al., 2014).

Other particles finer than 100 microns were probably blown away, but our simulations do not allow us to characterize their size or quantity. Although we cannot prove it, it is highly likely that particles smaller than 100 µm, including the dust fraction (5–10 µm), are contained in the regolith, similar to what has been observed in isolated aeolian bedforms and interdunes in Gale crater (e.g., Weitz et al., 2018, 2022) or in the regolith at the Phoenix landing site, where silt particles (10–60 µm) were observed (e.g., Goetz et al., 2010). The dust devil tracks observed in the surrounding plains (Lorenz, Lemmon, & Maki, 2021; Lorenz, Martínez, et al., 2021; Perrin et al., 2020) might also confirm the presence of dust in the regolith.

Conversely, calculations also showed that the largest particles deposited close to the tether at a distance of 10 cm have diameters comprised between 370 and 900 µm. We cannot either determine the GSD of those coarser grains in the piles, about which we only know the global proportion (~60% of scoop content before dump). Based on our theoretical calculations, the regolith in the piles is supposed to be coarser (>900 µm) than that initially scraped by the scoop. Note however that the real particle segregation due to wind sorting during dumping might be less severe than that calculated due to some simplistic hypothesis of the models, as discussed below. The three GSDs derived from wind speeds around 5 m.s$^{-1}$ (dumps 3, 4 and 6) are comparable, whereas that under 7 m.s$^{-1}$ (dump 4) provides a somewhat coarser GSD with a dominant grain population with a diameter around 170 µm, perhaps indicating some local heterogeneity of the scrapped regolith. The three other dumps provide finer GSDs showing well sorted materials with dominant diameters around 150 µm (dump 3), 138 µm (dump 4) and 119 µm (dump

6). These diameters are a little bit finer than those inferred previously (170 μm, e.g., Golombek et al., 2018) from orbital thermal inertia measurements (160 and 230 J $m^{-2}$ $K^{-1}$ $s^{-1/2}$, see Spohn et al. (2018)) but quite similar to that derived from InSight radiometer measurements (183 ± 25 J $m^{-2}$ $K^{-1}$ $s^{-1/2}$, Grott et al., 2021; Mueller et al., 2021; Piqueux et al., 2021; Spohn, Hudson, Marteau, et al., 2022; Spohn, Hudson, Witte, et al., 2022) corresponding to very fine to fine sand with a majority of particles smaller than 140 μm (Piqueux et al., 2021).

These values are consistent with those measured on various martian granular aeolian bedforms (ripples and dunes) from orbiters (e.g., Lane & Christensen, 2013; Rogers & Bandfield, 2009) and from cameras onboard rovers with sufficient resolution (e.g., Ehlmann et al., 2017; Gough et al., 2021; Jerolmack et al., 2006; Sullivan et al., 2005, 2008; Sullivan & Kok, 2017; Weitz et al., 2018, 2022). These investigations have demonstrated that most of the Martian aeolian bedforms observed are composed of 50 to 2,000 μm subrounded/rounded grains, with a preferential range of 50–350 μm for mobile grains in active ripples. The absence of bedforms and ripples in the vicinity of the InSight lander suggests that these particles are not mobilizable by the wind at this site because of their shape, the presence of smaller particles, or because their quantity is not sufficient to create aeolian bedforms. Note however that small displacements of individual coarse grains during gusts were observed (Baker et al., 2021; Charalambous et al., 2021).

The physical hypotheses adopted in both models are simplistic, in particular that of having spherical particles. However, this approximation appears reasonable, given the sub-rounded/rounded shape of fine regolith grains on Mars (e.g., Goetz et al., 2010; Weitz et al., 2018, 2020, 2022). In the models, we only considered the effects of gravity, buoyancy and drag force on individual grains, neglecting any (a) Possible mechanical interactions between grains (shocks/collision) during the fall; (b) Interactions of grains on the gas; (c) Wall effects. Nevertheless, the granulometry estimation is focused on particles blown, that is, particles separated by a distance greater than their diameter, which makes our hypothesis reasonable. However, one can expect that, in particular due to wall effects, piles contain smaller particles than what we calculated (>900 μm). This should not significantly affect the relative distribution of free particles blown and deposited in the plume. Moreover, the mechanical interaction between grains when they touch the ground has not been taken into account either. This can promote the mechanism of grain saltation and the detachment of fine particles (dust) aggregated with coarser grains releasing them into the atmosphere (e.g., Greeley, 2002; Musiolik et al., 2018). However, neglecting grain/grain and grain/gas interactions could be the reason why the plumes modeled by CFD are thinner than those observed since interactions could result in more grain dispersion and larger plumes. Note, however, that the critical characteristic of the plume, depending on the particle size distribution, is the length, that has been successfully modeled by both approaches. Wind speed and direction are measured by the TWINS sensors of the lander (about 1.2 m above the ground and 1.3 m away from the scoop). Wind data could be somewhat different at the scoop level during pouring because of turbulence caused by the lander and the various instruments (seismometer, $HP^3$, IDA…), resulting in lateral spreading of the grains at the surface.

In our models, we considered that the composition of the grains was essentially basaltic with a grain density of 3,000 $kg.m^{-3}$. This may appear restrictive with respect to the chemical and mineralogical compositions of regolith at other Martian sites (e.g., Berger et al., 2016; Weitz et al., 2022) where fine grains could easily self-aggregate. Sand-sized dust aggregates, much lighter due to their porous nature, could represent a non-negligible fraction of surface materials. But, since their fraction is not constrained at the InSight landing site, we preferred not to take it into account in our models.

An unknown parameter in our estimation is the value of the expansion coefficient $\alpha$ that characterizes the change in volume between the intact regolith and that extracted in the scoop. It depends on the various states met in the various processes, for example, intact, scraped into the scoop, poured onto the pile for the larger particles, blown and deposited in the plumes for medium-sized particles and finally blown away for the smallest particles below 100 μm. For current soils excavated on the Earth (densities between 1,500–1,700 $kg.m^{-3}$), a 10% expansion is adopted in earthwork calculations. In our case, only the granular upper 1 cm thick unconsolidated layer was scraped (see Figure 5). As a consequence, it seems reasonable to consider that the scraped regolith in the scoop has a density close to that of the initial cohesionless upper layer, with no expansion ($\alpha = 1$).

## 5. Conclusion

The tether covering operations, initiated by the InSight Science Team to improve the quality of the signal provided by the SEIS seismometer, showed that a non-negligible fraction of the regolith poured from the IDA

scoop at heights around 45 cm did not reach the tether. More detailed observation and analysis of the ICC images evidenced, by image differentiating, that a plume of blown particles was observed downwind of each pouring, the stronger the wind, the longer the plume. It was then decided to better constrain the GSD of the regolith by using the wind as a natural sorter, able to blow finer particles further.

The physical laws governing the phenomenon are relatively simple, and the effects of the various forces acting on the particles (gravity, buoyancy and drag) could be modeled through two approaches: a simpler one based on the MATLAB—SIMULINK tool, and another one using a Computational Fluid Dynamic tool. Both methods somewhat oversimplify the process, with no account of possible mutual interactions between the poured particles during the fall under the wind action.

For the 4 analyzed dumps, both methods provided comparable results in terms of plume orientation and length, confirming the validity of the approach through two different models. A satisfactory modeling of the trajectories of the particles blown by the wind was achieved in both cases. However, the modeled plumes appeared to be thinner than the observed plumes, probably because of neglecting the particle mutual interactions during the fall together with the effect of the gas. It was observed that the largest particles blown and deposited closer to the tether (around 10 cm for dumps #4 and #6) had a diameter of 900 μm, whereas the finest ones blown at the extremity of the plume (between 3 and 4 m) had a diameter of 115 μm, not far from that previously estimated from thermal inertia measurements (average diameter of 170 μm).

The analysis presented in this paper makes it possible to refine the estimation of the GSD of the Martian regolith from an experiment of opportunity. In spite of some limitations, particularly concerning the fraction of smallest particles blown away by the wind that cannot be estimated, one can consider that this promising technique could be further developed for future missions on Mars. Some improvements could be implemented, in particular with respect to better characterize the plumes by cameras. It would be good to use a high-resolution camera allowing a direct vertical shot above the plume in order to limit deformations. Further tests under other wind conditions (not possible on Insight due to the lack of energy) could also make it possible to explore other size ranges with smaller particles analyzed through smaller winds. Filming the deposits could also be interesting, since visualizing the particle trajectory would allow a recalibration of the model, and perhaps an estimate of the quantity of grains deposited outside the field.

## Data Availability Statement

The authors acknowledge NASA, UK Space Agency, CNES, their partner agencies and Institutions (UKSA, IC, SSO, DLR, JPL, IPGP-CNRS, ETHZ, and MPS-MPG) and the flight operations team at JPL, SISMOC, MSDS, IRIS-DMC, and PDS for acquiring and providing InSight data, including SEED SEIS data. InSight Lander camera images are publicly available through the IDC/ICC Bundle (Deen et al., 2019) and through the NASA Planetary Data System (PDS) Geosciences node and MarsInSight mission. The atmospheric measurement data presented here are also publicly available in the APSS TWINS Bundle (Mora, 2019). Seismic raw data are in "InSight Mars SEIS Data Service (2019a) *together with IPGP*, *JPL*, *CNES*, *ETHZ*, *ICL*, *MPS*, *ISAE-Supaero*, *LPG*, *MFSC*" (2019) and Insight Mars SEIS Data Service (2019b) SEIS Bundle.

**Acknowledgments**
The authors also thank the JGR Editor Laurent Montési, associate editor German Martinez and both the anonymous referees for their insightful suggestions and constructive review on greatly improving this manuscript. This work was supported by the French space agency, Centre National d'Etudes Spatiales (CNES). Portions of the research were carried out at the Jet Propulsion Laboratory, California Institute of Technology, under a contract with the National Aeronautics and Space Administration (80NM0018D0004). This paper is InSight Contribution Number 230.

## References

Abarca, H., Deen, R., Hollins, G., Zamani, P., Maki, J., Tinio, A., et al. (2019). Image and data processing for InSight lander operations and science. *Space Science Reviews*, *215*(2), 22. https://doi.org/10.1007/s11214-019-0587-9

Amsden, A., O'Rourke, P., & Butler, T. (1989). *KIVA-II: A computer program for chemically reactive flows with spray*. Los Alamos National Laboratory. https://doi.org/10.2172/6228444

Andreotti, B., Claudin, P., Iversen, J. J., Merrison, J. P., & Rasmussen, K. R. (2021). A lower-than-expected saltation threshold at Martian pressure and below. *Proceedings of the National Academy of Sciences of the United States of America*, *118*(5), e2012386118. https://doi.org/10.1073/pnas.201238611

Baker, M., Newman, C., Charalambous, C., Golombek, M., Spiga, A., Banfield, D., et al. (2021). Vortex-dominated Aeolian activity at InSight's landing site, Part 2: Local meteorology, transport dynamics, and model analysis. *J Geophys ResPlanets*, *126*(4), e2020JE006514. https://doi.org/10.1029/2020JE006514

Banerdt, W. S., Smrekar, S., Banfield, D., Giardini, D., Golombek, M., Johnson, C. L., et al. (2020). Initial results from the InSight mission on Mars. *Nature Geoscience*, *23*(3), 183–189. https://doi.org/10.1038/s41561-020-0544-y

Banfield, D., Rodriguez-Manfredi, J. A., Rissel, C. T., Rowe, K. M., Leneman, D., Lai, H. R., et al. (2019). InSight auxiliary payload sensor suite (APSS). *Space Science Reviews*, *215*(4), 4. https://doi.org/10.1007/s11214-018-0570-x

Banfield, D., Spiga, A., Newman, C., Forget, F., Lemmon, M., Lorenz, R., et al. (2020). The atmosphere of Mars as observed by InSight. *Nature Geoscience*, *13*(3), 190–198. https://doi.org/10.1038/s41561-020-0534-0

Beish, J. (2023). A revised list of dust storms on Mars. A.L.P.O. Mars section. Retrieved from https://alpo-astronomy.org/jbeish/DustStorms.pdf

Berger, J. A., Schmidt, M. E., Gellert, R., Campbell, J. L., King, P. L., Flemming, R. L., et al. (2016). A global Mars dust composition refined by the Alpha-Particle X-ray Spectrometer in Gale Crater. *Geophysical Research Letters*, *43*(1), 67–75. https://doi.org/10.1002/2015GL066675

Boyd, A. S. (2018). *Sand deposit mapping and Aeolian morphologies as clues for identifying origins of in Aeolis Dorsa, Mars*. Master s theses, University of Tenesee. Retrieved from https://trace.tennessee.edu/utk_gradthes/5182

Burr, D. M., de Silva, S. L., Zimbelman, J. R., & Bridges, N. T. (2012). Aeolian dunes from volcaniclastic sediments: The Medusae Fossae formation, Mars, and Andean ignimbrites. In *Earth. 43rd lunar and planetary science conference*. Abstract #1692.

Cannon, K. M., Britt, D. T., Smith, T. M., Fritsche, R. F., & Batcheldor, D. (2019). Mars global simulant MGS-1: A rocknest-based open standard for basaltic Martian regolith simulants. *Icarus*, *317*(1), 470–478. https://doi.org/10.1016/j.icarus.2018.08.019

Chapman, S., & Cowling, T. G. (1970). *The mathematical theory of non-uniform gases*. Cambridge University Press.

Charalambous, C., McClean, J. B., Baker, M., Pike, W. T., Golombek, M., Lemmon, M., et al. (2021). Vortex-dominated Aeolian activity at InSight's landing site, Part 1: Multi-instrument observations, analysis, and implications. *Journal of Geophysical Research: Planets*, *126*(6). https://doi.org/10.1029/2020JE006757

Christensen, P. R., Jakosky, B. M., Kieffer, H. H., Malin, M. C., McSween, H. Y., Jr., Nealson, K., et al. (2004). The thermal emission imaging system (THEMIS) for the Mars 2001 Odyssey mission. *Space Science Reviews*, *110*(1/2), 85–130. https://doi.org/10.1023/B:SPAC.0000021008.16305.94

Deen, R., Abarca, H., Zamani, P., & Maki, J. (2019). InSight cameras bundle. [Dataset]. NASA Planetary Data System. https://doi.org/10.17189/1510484

Delage, P., Marteau, M., Vrettos, E., Golomek, M. P., Ansan, V., Banerdt, W. B., et al. (2022). The mechanical properties of the Martian soil at the InSight landing site. In *Proceedings of the 20th international conference on soil mechanics and geotechnical engineering*. Retrieved from https://hal.science/hal-03706564

Ehlmann, B. L., Edgett, K. S., Sutter, B., Achilles, C. N., Litvak, M. L., Lapotre, M. G. A., et al. (2017). Chemistry, mineralogy, and grain properties at Namib and high dunes, Bagnold dune field, Gale crater, Mars: A synthesis of Curiosity rover observations. *Journal of Geophysical Research: Planets*, *122*(12), 2510–2543. https://doi.org/10.1002/2017JE005267

ENGYS. (2022). HELYX: Open-source CFD for enterprise. Retrieved from https://engys.com/products/helyx

Garcia, R. F., Daubar, I. J., Beucler, E., Posiolova, L. V., Collins, G. S., Lognonné, P., et al. (2022). Newly formed craters on Mars located using seismic and acoustic wave data from InSight. *Nature Geoscience*, *15*(10), 774–780. https://doi.org/10.1038/s41561-022-01014-0

Giardini, D., Ceylan, S., Clinton, J., Lognonné, P., & Stahler, S. (2022). The seismicity of Mars observed by the NASA InSight mission. *European Review*, *30*(5), 639–656. https://doi.org/10.1017/S1062798722000254

Giardini, D., Lognonné, P., Banerdt, W. B., Pike, W. T., Christensen, U., Ceylan, S., et al. (2020). The seismicity of Mars. *Nature Geoscience*, *13*(3), 205–212. https://doi.org/10.1038/s41561-020-0539-8

Goetz, W., Pike, W. T., Hviid, S. F., Madsen, M. B., Morris, R. V., Hecht, M. H., et al. (2010). Microscopy analysis of soils at the Phoenix landing site, Mars: Classification of soil particles and description of their optical and magnetic properties. *Journal of Geophysical Research: Planets*, *115*(8), 1–23. https://doi.org/10.1029/2009JE003437

Golombek, M., Grott, M., Kargl, G., Andrade, J., Marshall, J., Warner, N., et al. (2018). Geology and physical properties investigations by the InSight Lander. *Space Science Reviews*, *214*(84), 84. https://doi.org/10.1007/s11214-018-0512-7

Golombek, M., Hudson, T., Bailey, P., Balabanska, N., Marteau, E., Charalambous, C., et al. (2023). Results from InSight robotic arm activities. *Space Science Reviews*, *219*(3), 20. https://doi.org/10.1007/s11214-023-00964-0

Golombek, M., Warner, N. H., Grant, J. A., Hauber, E., Ansan, V., Weitz, C. M., et al. (2020). Geology of the InSight landing site on Mars. *Nature Communications*, *11*, 1–11. https://doi.org/10.1038/s41467-020-14679-1

Golombek, M., Williams, N., Warner, N. H., Parker, T., Daubar, I., Williams, M. G., et al. (2020). Location and setting of the Mars InSight lander, instruments, and landing site. *Earth and Space Science*, *7*(10). https://doi.org/10.1029/2020EA001248

Gómez-Elvira, J., Armiens, C., Castañer, L., Domínguez, M., Genzer, M., Gómez, F., et al. (2012). REMS: The environmental sensor suite for the Mars Science Laboratory rover. *Space Science Reviews*, *170*(1–4), 583–640. https://doi.org/10.1007/s11214-012-9921-1

Gough, T. R., Hugenholtz, C. H., & Barchyn, T. E. (2021). Re-evaluation of large Martian ripples in Gale crater: Granulometric evidence for an impact mechanism and terrestrial analogues. *Journal of Geophysical Research: Planets*, *126*(12), e2021JE007011. https://doi.org/10.1029/2021JE007011

Gousbet, G., & Berlemont, A. (1999). Eulerian and Lagrangian approaches for predicting the behaviour of discrete particles in turbulent flows. *Progress in Energy and Combustion Science*, *25*(2), 133–159. https://doi.org/10.1016/S0360-1285(98)00018-5

Grant, J. A., Arvidson, R., Bell, J. F., 3rd, Cabrol, N. A., Carr, M. H., Christensen, P., et al. (2004). Surficial deposits at Gusev crater along spirit rover traverses. *Science*, *305*(5685), 807–817. https://doi.org/10.1126/science.1099849

Greeley, R. (2002). Saltation impact as a means for raising dust on Mars. *Planetary and Space Science*, *50*(2), 151–155. https://doi.org/10.1016/S0032-0633(01)00127-1

Grott, M., Spohn, T., Knollenberg, J., Krause, C., Hudson, T. L., Piqueux, S., et al. (2021). Thermal conductivity of the Martian soil at the InSight landing site from HP3 active heating experiments. *Journal of Geophysical Research: Planets*, *126*(7), e2021JE006861. https://doi.org/10.1029/2021JE006861

Hayward, R. K., Fenton, L. K., & Titus, T. N. (2014). Mars Global Digital Dune Database (MGD3): Global dune distribution and wind pattern observations. *Icarus*, *230*, 38–46. https://doi.org/10.1016/j.icarus.2013.04.011

Heet, T. L., Arvidson, R. E., Cull, S. C., Mellon, M. T., & Seelos, K. D. (2009). Geomorphic and geologic settings of the Phoenix Lander mission landing site. *Journal of Geophysical Research*, *114*, E00E04. https://doi.org/10.1029/2009JE003416

Insight Mars SEIS Data Service. (2019b). InSight SEIS data Bundle. [Dataset]. PDS Geosciences (GEO) Node. https://doi.org/10.17189/1517570

InSight Mars SEIS Data Service. (2019a). SEIS raw data, Insight Mission. IPGP, JPL, CNES, ETHZ, ICL, MPS, ISAE-Supaero, LPG, MFSC. [Dataset]. InSight Mars SEIS Data Service. https://doi.org/10.18715/SEIS.INSIGHT.XB_2016

Jerolmack, D. J., Mohrig, D., Grotzinger, J. P., Fake, D. A., & Watters, W. A. (2006). Spatial grain size sorting in eolian ripples and estimation of wind conditions on planetary surfaces: Application to Meridiani Planum, Mars. *Journal of Geophysical Research*, *111*(E12), E12S02. https://doi.org/10.1029/2005JE002544

Kerber, L., Head, J. W., Madeleine, J.-B., Forget, F., & Wilson, L. (2011). The dispersal of pyroclasts from Apollinaris Patera, Mars: Implications for the origin of the Medusae Fossae formation. *Icarus*, *216*(1), 212–220. https://doi.org/10.1016/j.icarus.2011.07.035

Kerber, L., Head, J. W., Madeleine, J.-B., Forget, F., & Wilson, L. (2012). The dispersal of pyroclasts from ancient explosive volcanoes on Mars: Implications for the friable layered deposits. *Icarus*, *219*(1), 358–381. https://doi.org/10.1016/j.icarus.2012.03.016

Khan, A., Ceylan, S., Van Driel, M., Giardini, D., Lognonné, P., Samuel, H., et al. (2021). Upper mantle structure of Mars from InSight seismic data. *Science*, *373*(6553), 434–438. https://www.science.org/doi/10.1126/science.abf2966

Knapmeyer-Endrun, B., Banerdt, W. B., Smrekar, S. E., Lognonné, P., Giardini, D., Beghein, C., et al. (2022). Mars from the InSight: Seismology beyond Earth. In R. Vacareanu & C. Ionescu (Eds.), *Progresses in European earthquake engineering and seismology. ECEES 2022. Springer proceedings in Earth and environmental sciences*. Springer. https://doi.org/10.1007/978-3-031-15104-0_5

Knapmeyer-Endrun, B., Panning, M. P., Bissig, F., Joshi, R., Khan, A., Kim, D., et al. (2021). Thickness and structure of the Martian crust from InSight seismic data. *Science*, *373*(6553), 438–443. https://doi.org/10.1126/science.abf8966

Kok, J. F. (2010). Difference in the wind speeds required for initiation versus continuation of sand transport on Mars: Implications for dunes and dust storms. *Physical Review Letters*, *104*(7), 074502. https://doi.org/10.1103/PhysRevLett.104.074502

Lane, M. D., & Christensen, P. R. (2013). Determining olivine composition of basaltic dunes in Gale Crater, Mars, from orbit: Awaiting ground truth from Curiosity. *Geophysical Research Letters*, *40*(14), 3517–3521. https://doi.org/10.1002/grl.50621

Lapeyre, R., Gaudin, E., Verdier, N., Yana, C., Hurst, K., Ali, K., et al. (2022). Burying SEIS tether – A very unique operation, from design to realization on Mars. *IAC-22. Paper #70038*. Retrieved from https://dl.iafastro.directory/event/IAC-2022/paper/70038/

Lapotre, M. G. A., & Rampe, E. B. (2018). Curiosity's investigation of the Bagnold Dunes, Gale crater: Overview of the two-phase scientific campaign and introduction to the special collection. *Geophysical Research Letters*, *45*(19), 10200–10210. https://doi.org/10.1029/2018GL079032

Lefort, A., Burr, D. M., Beyer, R. A., & Howard, A. D. (2012). Inverted fluvial features in the Aeolis-Zephyria Plana, western Medusae Fossae formation, Mars: Evidence for postformation modification. *Journal of Geophysical Research*, *117*(3), E03007. https://doi.org/10.1029/2011JE004008

Lognonné, P., Banerdt, W. B., Clinton, J., Garcia, R. F., Giardini, D., Knapmeyer, B., et al. (2023). Mars seismology. *Annual Review of Earth and Planetary Sciences*, *51*(1), 643–670. https://doi.org/10.1146/annurev-earth-031621-073318

Lognonné, P., Banerdt, W. B., Giardini, D., Pike, W. T., Christensen, U., Laudet, P., et al. (2019). SEIS: Insight's seismic experiment for internal structure of Mars. *Space Science Reviews*, *215*(1), 12. https://doi.org/10.1007/s11214-018-0574-6

Lognonné, P., Banerdt, W. B., Pike, W. T., Giardini, D., Christensen, U., Garcia, R. F., et al. (2020). Constraints on the shallow elastic and anelastic structure of Mars from InSight seismic data. *Nature Geoscience*, *13*(3), 213–220. https://doi.org/10.1038/s41561-020-0536-y

Lorenz, R., Lemmon, M., & Maki, J. (2021). First Mars year of observations with the InSight solar arrays: Winds, dust devil shadows, and dust accumulation. *Icarus*, *364*, 114468. https://doi.org/10.1016/j.icarus.2021.114468

Lorenz, R., Lemmon, M. T., & Maki, J. (2021). First Mars year of observations with the InSight Solar Arrays: Winds, dust devil shadows, and dust accumulation. *Icarus*, *364*, 114468. https://doi.org/10.1016/j.icarus.2021.114468

Lorenz, R., Martínez, G. M., Spiga, A., Vicente-Retortillo, A., Newman, C. E., Murdoch, N., et al. (2021). Lander and rover histories of dust accumulation on and removal from solar arrays on Mars. *Planetary and Space Science*, *207*, 105337. https://doi.org/10.1016/j.pss.2021.105337

Maki, J. N., Golombek, M., Deen, R., Abarca, H., Sorice, C., Goodsall, T., et al. (2018). The color cameras on the InSight Lander. *Space Science Reviews*, *214*(6), 105. https://doi.org/10.1007/s11214-018-0536-z

Mandt, K. E., de Silva, S. L., Zimbelman, J. R., & Crown, D. A. (2008). The origin of the Medusae Fossae formation, Mars: Insights from a synoptic approach. *Journal of Geophysical Research*, *113*(E12), E12011. https://doi.org/10.1029/2008JE003076

Marteau, E., Golombek, M., Vrettos, C., Delage, P., Williams, N. H., & Ansan, V. (2022). Soil strength properties derived from scraping and dumping activities at the InSight landing site on Mars. *53th LPSC*. Abstract#1523 Retrieved from https://www.hou.usra.edu/meetings/lpsc2022/pdf/1523.pdf

Moler, C. (1980). Design of an interactive matrix calculator, AFIPS '80 Proceedings of the May 19-22, 1980. In *National computer conference* (pp. 363–368). https://doi.org/10.1145/1500518.1500576

Moore, H. J., Bickler, D. B., Crisp, J. A., Eisen, H. J., Gensler, J. A., Haldemann, A. F., et al. (1999). Soil-like deposits observed by Sojourner, the Pathfinder rover. *Journal of Geophysical Research*, *104*(E4), 8729–8874. https://doi.org/10.1029/1998je900005

Moore, H. J., & Jakoski, B. M. (1989). Viking landing sites, remote-sensing observations, and physical properties of Martian surface materials. *Icarus*, *81*(1), 164–184. https://doi.org/10.1016/0019-1035(89)90132-2

Mora, L. (2019). APSS TWINS data. Atmospheres Node. [Dataset]. NASA Planetary Data System. https://doi.org/10.17189/1518950

Mueller, N., Piqueux, S., Lemmon, M. T., Naki, J. N., Lorenz, R. D., Grott, M., et al. (2021). Near surface properties of Martian regolith derived from InSight HP³-RAD temperature observations during Phobos transits. *Earth and Space Science Open Archive*. https://doi.org/10.1002/essoar.10506920.1

Musiolik, G., Kruss, M., Demirci, T., Schrinski, B., Teiser, J., Daerden, F., et al. (2018). Saltation under Martian gravity and its influence on the global dust distribution. *Icarus*, *306*, 25–31. https://doi.org/10.1016/j.icarus.2018.01.007

Mutch, T. A., Grenander, S. U., Jones, K. L., Patterson, W., Arvidson, R. E., Guiness, E. A., et al. (1976). The surface of Mars: The view from the Viking 2 lander. *Science*, *194*(4271), 1277–1283. https://doi.org/10.1126/science.194.4271.1277

Nordin, P. (2001). *Ph.D Thesis. Complex chemistry modeling of diesel spray combustion*. Chalmers University of Technology. Retrieved from https://files.nequam.se/thesis.pdf

Perrin, C., Rodriguez, S., Jacob, A., Lucas, A., Spiga, A., Murdoch, N., et al. (2020). Monitoring of dust deviltracks around the InSight landingsite, Mars, and comparison with insitu atmospheric data. *Geophysical Research Letters*, *47*(10), e2020GL087234. https://doi.org/10.1029/2020GL087234

Piqueux, S., Müller, N., Grott, M., Siegler, M., Millour, E., Forget, F., et al. (2021). Soil thermophysical properties near the InSight lander derived from 50 sols of radiometer measurements. *Journal of Geophysical Research: Planets*, *126*(8), e2021JE006859. https://doi.org/10.1029/2021JE006859

Posiolova, L. V., Lognonne, P., Banerdt, W. B., Clinton, J., Collins, G. S., Kawamura, T., et al. (2022). Largest recent impact craters on Mars: Orbital imaging and surface seismic co-investigation. *Science*, *378*(6618), 412–416. https://doi.org/10.1126/science.abq7704

Rogers, A. D., & Bandfield, J. L. (2009). Mineralogical characterization of Mars Science Laboratory candidate landing sites from THEMIS and TES data. *Icarus*, *203*(2), 437–453. https://doi.org/10.1016/j.icarus.2009.04.020

Scholz, J.-R., Widmer-Schnidrig, R., Davis, P., Lognnoné, P., Pinot, B., Garcia, R. F., et al. (2020). Detection, analysis, and removal of glitches from InSight's seismic data from Mars. *Earth and Space Science*, *7*(11). https://doi.org/10.1029/2020EA001317

Scott, D. H., & Tanaka, K. L. (1986). Geologic map of the western equatorial region of Mars. *United States Geological Survey, Geologic Investigations Series Map I-1802-A*. https://doi.org/10.3133/i1802A

Shorthill, R. W., Moore, H. J., Scott, R. F., Hutton, R. E., Liebes, S., Jr., & Spitzer, C. R. (1976). The "soil" of Mars (Viking I). *Science*, *194*(4260), 91–97. https://doi.org/10.1126/science.194.4260.91

Spiga, A., Banfield, D., Teanby, N. A., Forget, F., Lucas, A., Kenda, B., et al. (2018). Atmospheric science with InSight. *Space Science Reviews*, *214*(109), 109. https://doi.org/10.1007/s11214-018-0543-0

Spiga, A., Murdoch, N., Lorenz, R., forget, F., Newman, C., Rodriguez, S., et al. (2021). A study of daytime convective vortices and turbulence in the Martian planetary boundary layer based on half-a-year of InSight atmospheric measurements and large-eddy simulations. *Journal of Geophysical Research: Planets*, *126*(1), e2020JE006511. https://doi.org/10.1029/2020JE006511

Spohn, T., Grott, M., Smrekar, S. E., Knollenberg, J., Hudson, T. L., Krause, C., et al. (2018). The heat flow and physical properties package (HP3) for the InSight mission. *Space Science Reviews*, *214*(96), 96. https://doi.org/10.1007/s11214-018-0531-4

Spohn, T., Hudson, T., Witte, L., Wippermann, T., Winnieski, L., Kedziora, B., et al. (2022). The InSight HP3 mole on Mars: Lessons Learned from attempts to penetrate to depth in the Martian soil. *Advanced Space Research*, *69*(8), 3140–3163. https://doi.org/10.1016/j.asr.2022.02.009

Spohn, T., Hudson, T. L., Marteau, E., Golombek, M., Wippermann, T., Ali, K. S., et al. (2022). The HP3 penetrator (Mole) on Mars: Soil properties derived from the penetration attempts and related activities. *Space Science Reviews*, *218*(72), 72. https://doi.org/10.1007/s11214-022-00941-z

Stähler, S. C., Khan, A., Banerdt, W. B., Lognonné, P., Giardini, D., Ceylan, S., et al. (2021). Seismic detection of the Martian core. *Science*, *373*(6553), 443–448. https://doi.org/10.1126/science.abi7730

Stokes, G. G. (1845). On the theories of the internal friction of fluids in motion. In *Transactions of the Cambridge philosophical society* (Vol. 8, pp. 287–305). Cambridge Philosophical Society.

Sullivan, R., Arvidson, R., Bell, J. F., Gellert, R., Golombek, M., Greeley, R., et al. (2008). Wind-driven particle mobility on Mars: Insights from Mars exploration rover observations at "El Dorado" and surroundings at Gusev crater. *Journal of Geophysical Research*, *113*(E6), E06S07. https://doi.org/10.1029/2008JE003101

Sullivan, R., Banfield, D., Bell, J. F., Calvin, W., Fike, D., Golombek, M., et al. (2005). Aeolian processes at the Mars exploration rover Meridiani Planum landing site. *Nature*, *436*(7047), 58–61. https://doi.org/10.1038/nature03641

Sullivan, R., & Kok, J. F. (2017). Aeolian saltation on Mars at low wind speeds. *Journal of Geophysical Research: Planets*, *122*(10), 2111–2143. https://doi.org/10.1002/2017JE005275

Sutherland, W. (1893). The viscosity of gases and molecular force. *The London, Edinburgh and Dublin Philosophical Magazine and Journal of Science*, *36*(223), 507–531. https://doi.org/10.1080/14786449308620508

Trainer, M. G., Wong, M. H., McConnochie, T. H., Franz, H. B., Atreya, S. K., Conrad, P. G., et al. (2019). Seasonal variations in atmospheric composition as measured in Gale Crater, Mars. *Journal of Geophysical Research: Planets*, *124*(11), 3000–3024. https://doi.org/10.1029/2019JE006175

Trebi-Ollennu, A., Kim, W., Ali, K., Khan, O., Sorice, C., Bailey, P., et al. (2018). InSight Mars lander robotics instrument deployment system. *Space Science Reviews*, *214*(93), 93. https://doi.org/10.1007/s11214-018-0520-7

Viviano, C., Murchie, S. L., Daubar, I. J., Morgan, M. F., Seelos, F. P., & Plescia, J. B. (2019). Composition of Amazonian volcanic materials in Tharsis and Elysium, Mars, from MRO/CRISM reflectance spectra. *Icarus*, *328*, 274–286. https://doi.org/10.1016/j.icarus.2019.03.001

Ward, J. G., Arvidson, R. E., & Golombek, M. (2005). The size-frequency and areal distribution of rock clasts at the Spirit landing site, Gusev Crater, Mars. *Geophysical Research Letters*, *32*(11), L11203. https://doi.org/10.1029/2005GL022705

Warner, N. H., Golombek, M. P., Ansan, V., Marteau, E., Williams, N., Grant, J. A., et al. (2022). In situ and orbital stratigraphic characterization of the InSight landing site—A type example of a regolith-covered lava plain on Mars. *Journal of Geophysical Research: Planets*, *127*(4), e2022JE007232. https://doi.org/10.1029/2022JE007232

Warner, N. H., Grant, J. A., Wilson, S. A., Golombek, M. P., DeMott, A., Charalambous, C., et al. (2020). An impact crater origin for the InSight landing site at Homestead hollow, Mars: Implications for near surface stratigraphy, surface processes, and erosion rates. *Journal of Geophysical Research: Planets*, *125*(4), e2019JE006333. https://doi.org/10.1029/2019je006333

Weitz, C. M., Anderson, R. C., Bell, J. F., III., Farrand, W. H., Herkenhoff, K. E., Johnson, J. R., et al. (2006). Soil grain analyses at Meridiani Planum, Mars. *Journal of Geophysical Research*, *111*(E12), E12S04. https://doi.org/10.1029/2005JE002541

Weitz, C. M., Grant, J. A., Golombek, M. P., Warner, N. H., Hauber, E., Ansan, V., et al. (2020). Comparison of InSight Homestead hollow to hollows at the Spirit landing site. *Journal of Geophysical Research: Planets*, *125*(7), e2020JE006435. https://doi.org/10.1029/2020JE006435

Weitz, C. M., O'Connell-Cooper, C., Thompson, L., Sullivan, R. J., Baker, M., & Grant, J. A. (2022). The physical properties and geochemistry of grains on Aeolian bedforms at Gale crater, Mars. *Journal of Geophysical Research: Planets*, *127*(11), e2021JE007061. https://doi.org/10.1029/2021JE007061

Weitz, C. M., Sullivan, R. J., Lapotre, M. G. A., Roland, S. K., Grant, J. A., Baker, M., & Yingst, R. A. (2018). Sand grain sizes and shapes in eolian bedforms at Gale Crater Mars. *Geophysical Research Letters*, *45*(18), 9471–9479. https://doi.org/10.1029/2018GL078972

Wentworth, C. K. (1922). A scale of grade and class terms for clastic sediments. *The Journal of Geology*, *30*(5), 337–424. https://doi.org/10.1086/622910

Yana, C., Hurst, K., Kerjean, L., Gaudin, E., Lognonné, P., Rochas, L., et al. (2021). InSight-SEIS instrument deployment operations on Mars. In *Proceeding of 16th international conference on space operations* (Vol. 787–804). Retrieved from https://www.proceedings.com/content/064/064766webtoc.pdf

Yana, C., Lapeyre, R., Gaudin, E., Hurst, K., Lognonné, P., & Rochas, L. (2023). Deployment and surface operations of the SEIS instrument onboard the InSight mission. *Acta Astronautica*, *202*, 772–781. https://doi.org/10.1016/j.actaastro.2022.10.010

Yingst, R. A., Haldemann, A. F. C., Biedermann, K. L., & Monhead, A. M. (2007). Quantitative morphology of rocks at the Mars Pathfinder landing site. *Journal of Geophysical Research*, *112*(E6), E06002. https://doi.org/10.1029/2005JE002582

Yingst, R. A., Kah, L. C., Palucis, M., Williams, R. M. E., Garvin, 1 J., Bridges, J. C., et al. (2013). Characteristics of pebble-and cobble-sized clasts along the Curiosity rover traverse from Bradbury Landing to Rocknest. *Journal of Geophysical Research: Planets*, *118*(11), 2361–2380. https://doi.org/10.1002/2013JE004435

Zimbelman, J. R., & Griffin, L. (2010). HiRISE images of yardangs and sinuous ridges in the lower member of the Medusae Fossae Formation, Mars. *Icarus*, *205*(1), 198–210. https://doi.org/10.1016/j.icarus.2009.04.003